Two-Metal-Ion Mechanism for Hammerhead-Ribozyme Catalysis

Fabrice Leclerc, Martin Karplus

Two-Metal-Ion Mechanism for Hammerhead-Ribozyme Catalysis

Fabrice Leclerc*,†,‡,§ and Martin Karplus*,‡,§

Laboratoire de Maturation des ARN et Enzymologie Moléculaire, Université Henri Poincaré, Faculté des Sciences, B.P. 239, Bd. des Aiguillettes, 54506 Vandoeuvre-lès-Nancy, France, Department of Chemistry and Chemical Biology, Harvard University, 12 Oxford Street, Cambridge, Massachusetts 02138, and Laboratoire de Chimie Biophysique, Université Louis Pasteur, Institut le Bel, 67000 Strasbourg, France

Received: July 12, 2005; In Final Form: November 2, 2005

The hammerhead ribozyme is one of the best studied ribozymes, but it still presents challenges for our understanding of RNA catalysis. It catalyzes a transesterification reaction that converts a 5′,3′ diester to a 2′,3′ cyclic phosphate diester via an S_N2 mechanism. Thus, the overall reaction corresponds to that catalyzed by bovine pancreatic ribonuclease. However, an essential distinguishing aspect is that metal ions are not involved in RNase catalysis but appear to be important in ribozymes. Although various techniques have been used to assign specific functions to metals in the hammerhead ribozyme, their number and roles in catalysis is not clear. Two recent theoretical studies on RNA catalysis examined the reaction mechanism of a single-metal-ion model. A two-metal-ion model, which is supported by experiment and based on ab initio and density functional theory calculations, is described here. The proposed mechanism of the reaction has four chemical steps with three intermediates and four transition states along the reaction pathway. Reaction profiles are calculated in the gas phase and in solution. The early steps of the reaction are found to be fast (with low activation barriers), and the last step, corresponding to the departure of the leaving group, is rate limiting. This two-metal-ion model differs from the models proposed previously in that the two metal ions function not only as Lewis acids but also as general acids/bases. Comparison with experiment shows good agreement with thermodynamic and kinetic data. A detailed analysis based on natural bond orbitals (NBOs) and natural energy decomposition (NEDA) provides insights into the role of metal ions and other factors important for catalysis.

1. Introduction

The discovery of catalytic RNA molecules (ribozymes) in the early 1980s,[1,2] at a time when proteins were thought to be the only enzymes, raised the fundamental question of how RNA enzymes work. Although ribozymes have been under intense study for the intervening years, no mechanism that provides a detailed description of the reaction is universally accepted for any ribozyme. Among the various known RNA enzymes, the best-characterized is the hammerhead ribozyme. It was the first ribozyme to be crystallized, and a series of X-ray structures corresponding to a biologically active ribozyme have been determined.[3−6] This ribozyme has also been the subject of numerous biochemical studies, yet questions remain regarding the reaction mechanism.[7−9] Like the RNA-catalyzed self-cleavage of other ribozymes,[10] the reaction catalyzed by the hammerhead ribozyme involves a transesterification step in the phosphate ester hydrolysis.[11] This step leads to isomerization from a 5′,3′ diester to a 2′,3′ cyclic phosphate diester. In a second step, the 2′,3′ cyclic phosphate is hydrolyzed to yield a 3′ phosphate and regenerate the 2′ OH group. The transesterification reaction has been shown to proceed via an $S_N2(P)$ or "in-line" mechanism in which the attacking nucleophile (the 2′ oxygen) is aligned with the phosphorus atom and the 5′ oxygen atom of the phosphate group from the neighboring 3′ nucleotide.[12−14] Thus, the overall mechanism corresponds to that found in bovine pancreatic RNase,[15] although metal ions, which appear to play an essential role for the ribozymes, are not present in RNase. Models proposed for the reaction mechanism differ particularly with respect to the number of metal ions involved (single-metal-ion mechanisms[16−20] or two-metal-ion mechanisms[21,22]) and their specific role in the catalysis; that is, whether they act as a general acid/base, an electrophilic catalyst, or a Lewis acid[19] (Figure 1). When the metal is involved in the deprotonation of a nucleophile or in the protonation of a leaving group, it can function either as a Lewis acid or as a generalized acid/base. The metal acts as a Lewis acid if it stabilizes an anionic nucleophile or leaving group (by direct coordination of the metal to the oxygens of the phosphate group) but does not participate directly in the proton transfer, while it acts as a general acid or base when it is directly involved as a proton donor (from hydrated metal) or acceptor (by metal hydroxide). The metal functions as an electrophilic catalyst when it activates the electrophile (the phosphorus atom) by making it more susceptible to nucleophilic attack (by direct coordination of the metal to the nonbridging pro-R or pro-S oxygens). The single-metal-ion mechanisms are mostly based on a general acid/base model of catalysis (Figure 1B), while the two-metal-ion mechanisms are mostly based on a Lewis acid model of catalysis (Figure 1C and D). The experimental data, originally supporting a single-metal-ion mechanism (Figure 1A),[23−25] were shown subsequently to be more consistent with a two-metal-ion mechanism (Figure 1B and C).[26] Since then, additional experimental evidence has accumulated in favor of a two-metal-ion

* To whom correspondence should be addressed. E-mail: fabrice.leclerc@maem.uhp-nancy.fr (F.L.); marci@tammy.harvard.edu (M.K.).
† Université Henri Poincaré.
‡ Harvard University.
§ Université Louis Pasteur.

10.1021/jp053835a CCC: $33.50
Published on Web 02/01/2006 PAGE EST: 14.3

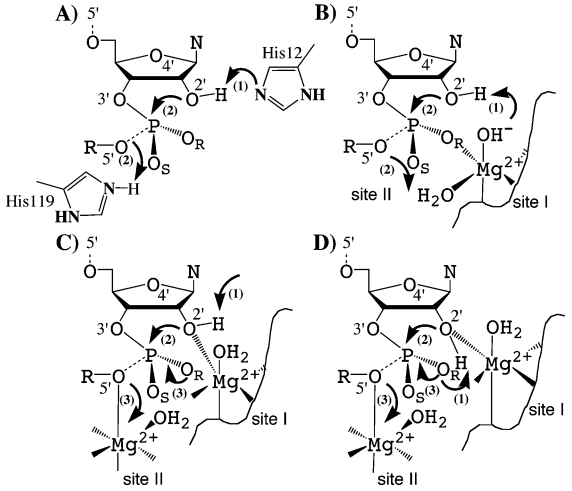

Figure 1. General acid/base catalysis vs metal-ion catalysis in the transesterification step of RNA hydrolysis. (A) General acid/base mechanism in RNase A. In this model, His12 acts as a general base to activate the 2′ oxygen as the nucleophile by abstraction of the proton from the 2′ OH (1), while His119 acts as a general acid to facilitate the departure of the leaving group by protonation of the 5′ oxygen (2). (B) General acid/base mechanism in the hammerhead ribozyme. In this single-metal-hydroxide-ion model,[16−20] the metal hydroxide (site I) activates the 2′ oxygen as the nucleophile (1). The activated 2′ oxygen attacks the phosphorus and induces the departure of the 5′ oxygen leaving group (2). The hydrated metal (site II) can be regenerated as a cofactor by giving away a proton from a coordinated water molecule to the 5′ oxygen (2). (C) Metal-ion catalysis in the hammerhead ribozyme. In this two-metal-ion model based on the dianionic mechanism,[24−28] an external Brönsted base (water molecule) activates the 2′ oxygen (1). The attack of the 2′ oxygen on the phosphorus (2) is followed by the departure of the leaving group (3). The metals at sites I and II act as Lewis acids by accepting the electrons from the 2′ and 5′ oxygens, respectively. (D) Alternative metal-ion catalysis in the hammerhead ribozyme. In this two-metal-ion model based on the triester-like mechanism (monoanionic mechanism),[25,37,52] the activation of the 2′ oxygen is accomplished by one of the nonbridging oxygens of the phosphate group that accepts the proton from the 2′ OH (1). The rest of the mechanism is similar to the mechanism in part B. The mechanisms in both parts B and C are shown as being sequential, though they could be concerted, in part.

mechanism.[27−30] The two-metal-ion mechanism is strongly supported by the differential metal-ion effects on the cleavage rate observed for the natural substrate (cleavage activation observed in the presence of Mg^{2+} and La^{3+})[28,30] and for a 5′ thio modified substrate.[27] The metal ions usually involved in chemical catalysis are divalent cations such as Mg^{2+} or Mn^{2+}. Recent studies have shown that monovalents cations, such as Na^+, Li^+, and NH_4^+, can also act as metal cofactors at extremely high concentrations (400-fold higher).[31−34] In fact, the hammerhead-catalyzed reaction is significantly more efficient in the presence of divalent ions that act as catalytic cofactors under physiological conditions. Even under more favorable but artificial conditions (hammerhead RNA with a small helix I domain and an extremely high concentration of monovalent ions), the rate enhancement in 4 M Li^+ is 10-fold less than that in 10 mM Mg^{2+}.[32,34] Studies where both divalent ions and monovalent ions are combined suggest that the divalent-metal-ion-catalyzed reaction may involve a Mg^{2+} ion with weak binding affinity in vivo;[35,36] this could explain why the difference in rate enhancement between the hammerhead cleavage reactions stimulated by monovalent ions and by divalent ions is not more significant in solution. In summary, since high concentrations of monovalent ions are inhibitory for the hammerhead ribozyme in cells,[35] all evidence points to the fact that the hammerhead cleavage reaction in vivo should follow a divalent-metal-ion-dependent channel,[35,36] as assumed here. Ribozymes can function by both base-catalyzed and acid-catalyzed mechanisms, depending on the pH of the solution. Both reaction mechanisms produce a 2′,3′ cyclic phosphate and a 5′ oxygen leaving group. The base-catalyzed reaction, which we consider here, is believed to involve a dianionic phosphorane species; the 2′ OH group is activated by an external base, which can be assisted by the direct coordination of a metal ion to the 2′ oxygen[29] to form a 2′ O^- oxyanion that attacks the adjacent phosphorus to generate the dianionic phosphorane.[25]

In the monoanionic or "triester-like" mechanism (based on a two-metal-ion model), the 2′ proton is transferred to the nonbridging phosphoryl oxygen (pro-Rp) to render the substrate triester-like. This latter mechanism was proposed to explain thio effects (loss of catalytic activity when substituting one of the nonbridging oxygens by sulfur) and rescue effects (restoration of catalytic activity by thiophilic metal ions) in hammerhead-catalyzed reactions.[37] SpS and RpS isomers of hammerhead-ribozyme substrates are much less reactive than the natural unmodified substrates (thio effect). The fact that the thio effect is much larger for the RpS isomer than the SpS isomer suggested the pro-Rp oxygen plays a more critical role. This would mean that the pro-Rp oxygen is the proton acceptor during the 2′ OH deprotonation. However, reinvestigation of the thio effect and rescue have shown that the data can be explained by the coordination of a divalent metal ion to the pro-Rp oxygen at the cleavage site.[38] The dianionic mechanism is also more consistent with other experimental data. Indeed, a pH-dependent conformational change of the hammerhead ribozyme associated with the chemical reaction suggests that a 2′ O^- oxyanion is formed by deprotonation of the 2′ OH group.[39] The deprotonation, taking place at basic pH (at or above pH 8.5), would drive the conformational change that initiates the reaction. Quantum mechanical studies of a small RNA model compound (a phosphorylated ribose with a 5′ O-methoxy group as the leaving group) and different phosphorothioate analogues also suggest there is no significant preference for the triester-like mechanism over the dianionic mechanism (Lopez et al., Leclerc et al., to be published). The calculated activation free energies in solution, with the unmodified analogue in the absence of metal ions, are 34.2 (Supporting Information Figure S1) and 22.9 kcal/mol (Supporting Information Figure S2) for the two mechanisms, respectively.

Although qualitative descriptions of the single- and two-metal-ion mechanisms have been available for some time,[23,24] a quantitative theoretical study of the reaction pathway for a single-ion mechanism was published only recently.[20] In the present paper, we propose a quantitative two-metal-ion model for the reaction mechanism of the transesterification step in the hammerhead catalysis. The study was guided by the insightful discussions of von Hippel and co-workers[26,28] of a two-metal-ion mechanism based on experimental data and a proposal of Steitz and Steitz[21] for a variety of protein and RNA enzymes that cleave phosphodiester bonds. The model was built from the small RNA model mentioned above by adding two solvated magnesium ions. Ab initio and density functional theory (DFT) methods were used to calculate the structures of the stationary points identified along the reaction path and the energetics (relative energy and free energy profiles) of the corresponding chemical processes using realistic quantum chemical models (including electron correlation effects and a large basis set) both in the gas phase and in solution. Reaction path calculations were performed for each transition state to ensure that it is connected to the corresponding starting and ending structures. The

TABLE 1: Geometries of Stationery Points on the Reaction Path for Transesterification of Methyl Ribose Phosphate[a]

	guess[b] 0	reactant I	TS1 II‡	intermediate 1 III	TS2 IV‡	intermediate 2 V	TS3 VI‡	intermediate 3 VII	TS4 VIII‡	product IX
P−O2′	2.845	2.805	2.817	2.766	2.167	1.916	1.829	1.783	1.708	1.607
H−O2′		1.035	1.131	2.487						
H(O2′)−O⁻(Mg$_I$)		1.538	1.321	0.971						
O2′−O⁻(Mg$_I$)		2.359	2.285	2.766						
P−O3′	1.555	1.559	1.556	1.560	1.589	1.614	1.609	1.614	1.599	1.604
P−O5′	1.730	1.606	1.607	1.620	1.663	1.692	1.697	1.709	2.027	2.955
P−O$_R$	1.533	1.548	1.549	1.549	1.566	1.581	1.592	1.590	1.554	1.531
P−O$_S$	1.476	1.478	1.479	1.478	1.489	1.499	1.519	1.530	1.497	1.475
Mg$_I$−O2′	1.946	2.075	2.031	1.832	1.886	1.939	1.954	1.992	2.096	2.763
Mg$_I$−O$_R$	2.050	1.968	1.963	2.019	1.999	1.978	1.948	2.013	1.999	2.027
Mg$_{II}$−O5′	2.146	2.310	2.317	2.215	2.215	2.105	2.067	1.998	2.204	2.101
Mg$_{II}$−O$_R$	2.057	1.972	1.965	1.994	1.980	1.978	1.948	2.000	1.999	2.027
Mg$_I$−Mg$_{II}$	3.910	3.700	3.702	3.866	3.873	3.857	3.768	3.850	3.768	3.685
Mg$_I$−OH$_2$[c]	2.273	4.782	4.762	4.688	4.524	4.450	3.649	2.079	2.038	2.578
O4′−OH[d]	1.763	1.578	1.567	1.545	1.583	1.617	1.660	1.631	1.605	1.616
O2′−P−O5′	140.1	161.6	161.3	157.2	162.1	162.9	160.7	165.6	163.7	157.5
O2′−H−O⁻(Mg$_I$)		131.8	137.4	96.23						

[a] Geometries optimized at the RHF/3-21+G* level. Distances are given in angstroms, and angles, in degrees. Numbers in italics correspond to significant variations in distance due to the change in protonation state of the 5′ oxygen associated with the departure of the leaving group. [b] Starting structure used as initial guess in the geometry optimizations (Figure 2). [c] Distance measured between the magnesium at the first metal site and the oxygen of the water molecule associated with the switch from a penta- to hexacoordinated magnesium. [d] Distance measured between the O4′ oxygen and the hydrogen of the water molecule associated with the switch from a penta- to hexacoordinated magnesium.

complete reaction path from the reactant, a 3′ phosphorylated ribose, to the product, a 2′,3′ cyclic phosphorylated ribose and a 5′ OH methyl leaving group, has been obtained. The results show the coordination of the metal ions along the transesterification pathway and demonstrate their role in catalysis, as well as the importance of solvent effects on the free energy profile of the reaction.

2. Model and Methods

The model used in this study is a phosphorylated ribose complexed with two hydrated magnesium cations. The model is based, in part, on the structures of two conformational intermediates of the hammerhead ribozyme obtained by crystallographic freeze-trapping: the "early" intermediate shows two Mg^{2+} ions in proximity to the cleavage site (one coordinated to the pro-Rp nonbridging phosphate oxygen and the second distant from the first one by 4.4 Å), in addition to three other Mg^{2+} ions that are further from the cleavage site;[3] the "late" intermediate shows a conformation compatible with an in-line attack mechanism.[6] The conformational changes associated with these two intermediates, relative to the "ground state" structure, are restricted to the catalytic pocket of the ribozyme. One of the metals is coordinated to the nonbridging pro-R oxygen of the phosphate group with a Mg^{2+}−O distance of 2.43 Å. In the proposed two-metal-ion model (see below), the stationary points exhibit geometries corresponding to an in-line mechanism involving a metal-to-metal distance between 3.69 and 3.87 Å and a metal-to-pro-R-oxygen distance between 1.95 and 2.0 Å (Table 1). Preliminary calculations on a model compound corresponding to a phosphorylated ribose allowed us to identify the stationary points and a unique transition state connecting the reactant and product of the transesterification step, in the base-catalyzed phosphate ester hydrolysis (Leclerc et al., to be published separately). In the absence of metal ions, the reaction follows a dianionic mechanism where the nucleophilic attack of the 2′ oxygen on the phosphorus is concerted with the departure of the 5′ oxygen leaving group. The geometry of the RNA part was taken from this transition state; this assumes that the metals stabilize the in-line conformation of the phosphorylated ribose, which corresponds to the active conformation in the catalytic pocket of the hammerhead ribozyme. Two solvated metal ions, hexa- or pentacoordinated, were added via inner-sphere coordinations with the 2′ oxygen and the 5′ oxygen, in accord with the proposed metal coordinations for the two-metal-ion model.[25,26,29] With these structural constraints, various penta- and hexacoordinated forms of hydrated magnesium ions[40] were constructed (a total of 10 geometries). After full optimization, some "guessed" geometries deviated significantly from their initial geometry while others preserved the in-line conformation ($\angle$(O2′−P−O5′) ≥ 140 °). Among those, several guessed geometries converged to the same or some equivalent conformation, which differs only by the number of solvating water molecules (for details, see the Supporting Information). In the case of equivalent conformations with the same metal inner-sphere coordinations, the more solvated ones were preferred. Finally, only conformations that exhibit conserved inner-sphere coordinations with the pro-Rp oxygen, as proposed in the two-metal-ion model,[25,26,29] were retained. Two nonequivalent in-line conformations with eight and nine water molecules in the metal coordination shells were selected after optimization. One of these, the conformation with eight water molecules (four water molecules in the coordination shell of each metal), inner-sphere coordination with the pro-Rp oxygen and 2′ oxygen at the first metal site and inner-sphere coordination with the pro-Rp oxygen and 5′ oxygen at the second metal site (Figure 2), was selected as the starting structure for the subsequent calculations. The model with nine water molecules attached to the metal ions was excluded because it has only a single inner-sphere coordination (the other is an outer-sphere coordination) with the pro-Rp oxygen, which is less consistent with experimental evidence.[28,41] Moreover, the distance between the two metal ions (more than 5.6 Å) in this model fit the X-ray data less well (distance between metal at sites 1 and 6 of 4.4 Å) than that with eight water molecules (3.9 Å, Table 1).

The geometry of the model structure, optimized at the HF/3-21+G* level, was used as the starting point for the reaction path calculations. The O2′−P and P−O5′ distances were used as the reaction coordinates; they correspond to the nucleophilic attack on the phosphorus and the departure of the leaving group, respectively. Nine geometries were generated with a distance range for the O2′−P and P−O5′ internal coordinates that include O2′−P bond formation (distance between 3.235 and 1.742 Å)

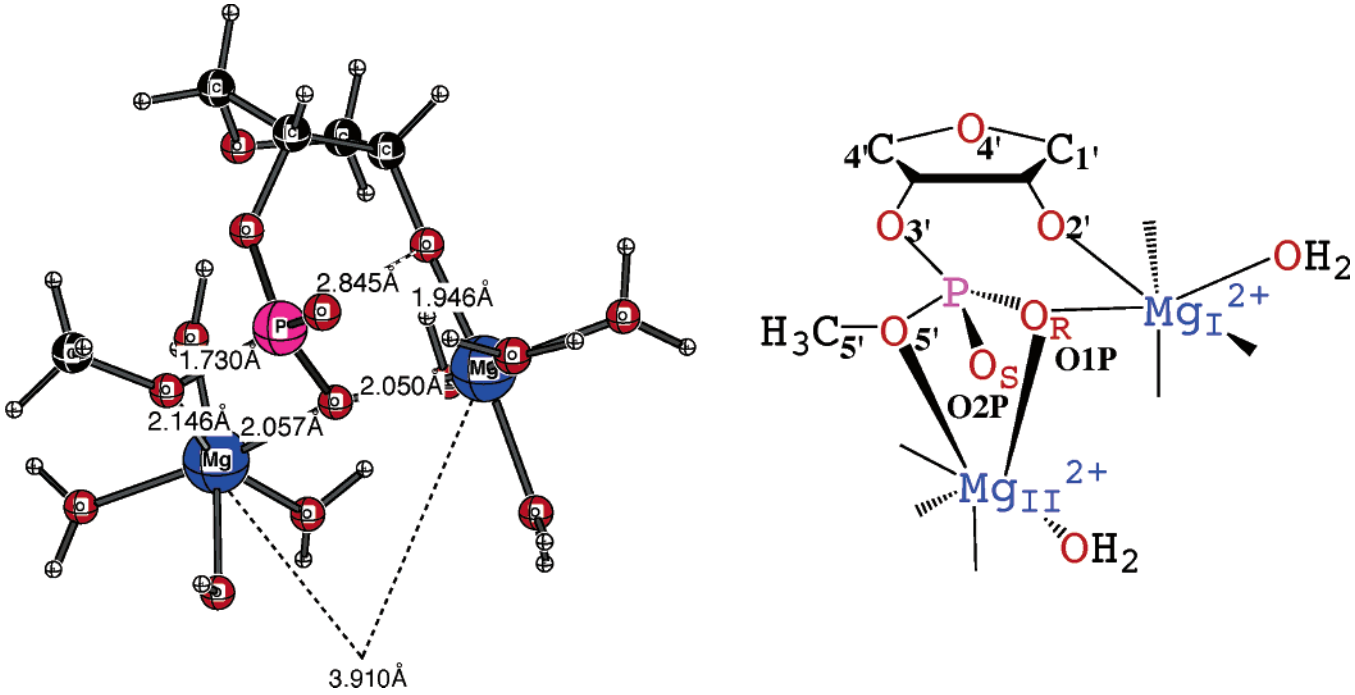

Figure 2. Model structure used to locate stationary points. The structure of the two-metal-ion model corresponding to the geometry optimized at the HF/3-21+G* level and its schematic representation with the stereochemistry of the nonbridging oxygens of the phosphate group are shown on the left and right sides, respectively. The atoms are colored according to the following code: carbon, black; hydrogen, white; oxygen, red; phosphorus, magenta; magnesium, blue.

and P−O5′ bond breaking (distance between 1.726 and 4.167 Å); the end points were chosen by following the reaction path (intrinsic reaction coordinate calculations) for the reaction of a phosphorylated ribose in the absence of metal ions (i.e., in the small RNA model mentioned above). Geometry optimizations and frequency calculations with O2′−P and P−O5′ frozen internal coordinates on those 10 geometries were then done to locate possible transition states corresponding to the nucleophilic attack, the departure of the leaving group, or both in the case of a concerted mechanism. Four out of the ten constrained geometries optimized at the HF/3-21+G* level had an imaginary frequency. After full relaxation (optimization and frequency calculations at the HF/3-21+G* level), only two geometries corresponded to transitions states: one to the nucleophilic attack and the other one to the departure of the leaving group. Reaction path following was performed from these transition states to determine the stationary points corresponding to possible intermediates. The stationary points corresponding to the 2′ OH activation were inferred from the intermediate (dianionic species) that just precedes the nucleophilic attack. In this way, five local minima corresponding to the reactant (R), product (P), and different intermediates along the reaction pathway (I1, I2, and I3) were obtained from the three saddle points (transition states) corresponding to the 2′ OH activation (TS1), the nucleophilic attack (TS2), and the departure of the leaving group (Table 1). The presence of more than (n + 1) local minima with respect to the number of saddle points indicated that a saddle point was missing along the reaction pathway. The synchronous transit-guided quasi-Newton (STQN) method was then used to locate this missing transition state, which connects the second and third intermediates (I2 and I3). The full reaction path involves nine stationary points: four transition states and three intermediates plus the reactant and the product. The free energies in the gas phase and solution of the stationary points relative to the reactant were calculated at the B3LYP/6-31+G**//HF/3-21+G* level (for details, see the Supporting Information).

All geometry optimizations were performed using Gaussian 98 (Gaussian, Inc., Pittsburgh, PA, 2001, revision A.10). The frequencies were scaled by an empirical factor of 0.9207 to correct, at the HF/3-21+G* level, for errors in the potential energy surface.[42] The vibrational contributions to the entropy and to the enthalpy, zero-point energy, and vibrational energy at 298 K were calculated from the frequencies. The other contributions (rotational and translational entropies and the work term (PV)) were calculated according to standard classical statistical mechanics (e.g., an ideal gas PV term was added to obtain the Gibbs free energy). Effective energies in solution were calculated for the geometries optimized in the gas phase using the solvation model (Poisson−Boltzmann solver) implemented in Jaguar (Jaguar, Schrödinger, Inc., 2002, version 4.2).[43] The eight explicit water molecules in the solvation shells of the two metals are treated as part of the solute in the solvation calculations. The use of a continuum model for the treatment of the solvation effects is based on the assumption that water molecules from the solvent do not modify the metal coordinations we have described. The assumption is supported by the results obtained with an explicit solvent model for each stationary point of the reaction path (Zdenek and Leclerc, data not shown). The latter used a combined quantum mechanical and molecular mechanical (QM/MM) method implemented in the CHARMM program interfaced with the ab initio quantum mechanical GAMESS program. Optimization of the geometry of each stationary point solvated in a 15 Å^3 waterbox resulted in geometries and coordinations very close to those obtained at the QM level in this paper (the maximum deviation is 0.07 Å for the bond length and 0.2 Å for the metal coordination).

3. Results

3.1. The Reaction Mechanism. The reaction is found to involve four chemical steps (Figure 3): (1) nucleophile activation (Figure 3A) to form a dianionic species (for comparison with the theoretical study published recently,[20] we have

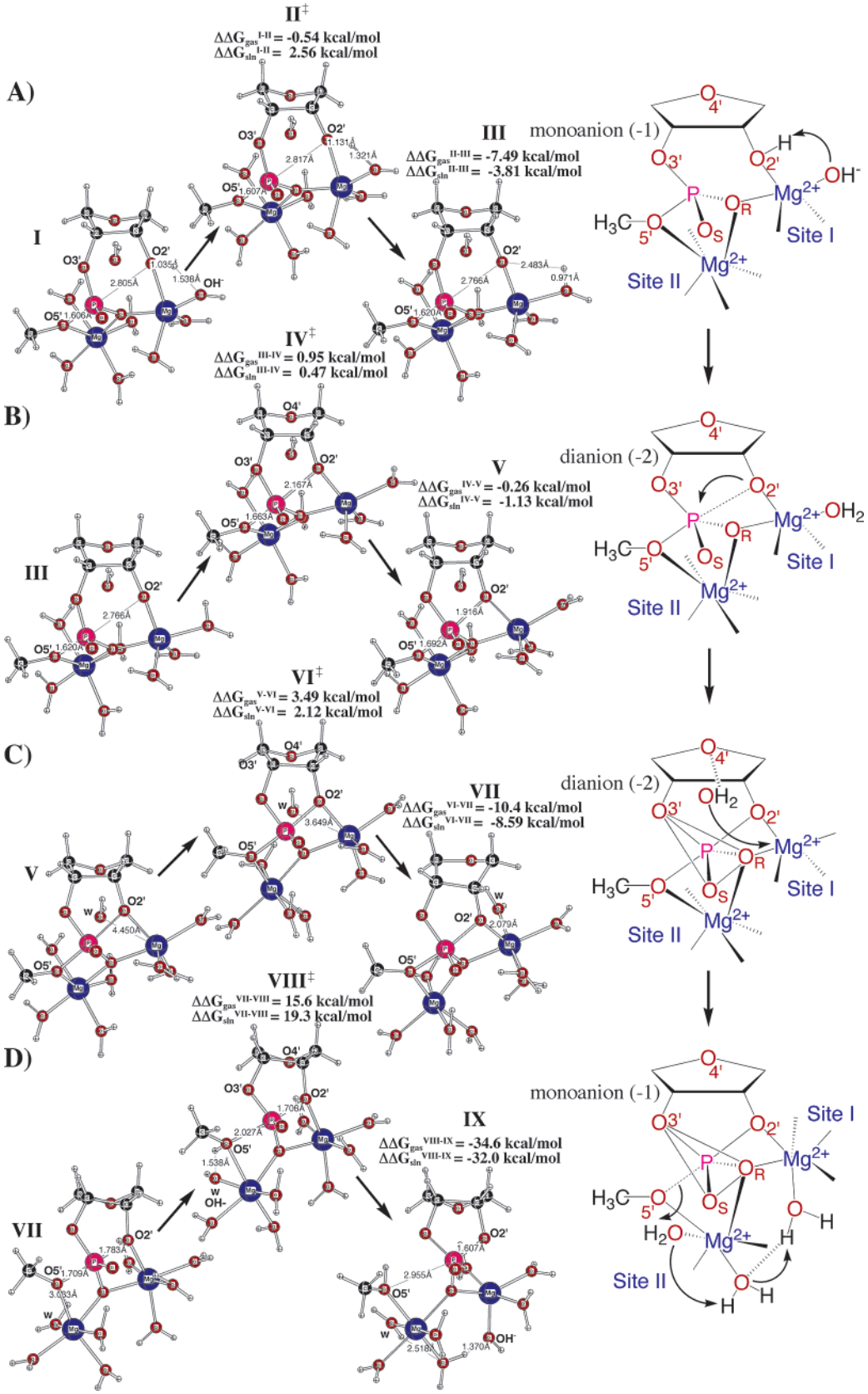

Figure 3. Proposed mechanism for hammerhead-catalyzed reactions. (A) First reaction step: nucleophile activation of the 2′ OH into a 2′ oxyanion. (B) Second reaction step: nucleophilic attack of the 2′ oxygen on the phosphorus. (C) Third reaction step: coordination change at the first metal site (site I). (D) Fourth reaction step: departure of the 5′ oxygen leaving group. The structures of the stationary points located along the reaction pathway are shown with indication of the forward and reverse energy barriers between each of them. The activation energies (backward and forward) are given at the B3LYP-6-31+G**//HF/3-21+G* level and at the HF/3-21+G* level in parentheses. Transition states are labeled by a double dagger. A set of distances relevant to each chemical step are indicated. The structures are represented with the atom color code used in the previous figure. A schematic representation (right side) shows the major features of each step: arrows indicate the bonding changes and dotted lines the bond formation or bond breaking.

TABLE 2: Relative Energies and Free Energies (at 298 K) for Stationery Points on the Transesterification Path of Methyl Ribose Phosphate with Respect to the Starting Molecule[a]

molecule[b]	ΔE	ΔZPE[c]	ΔE_{TRV}	$T\Delta S_{TRV}$	ΔG_{gas}[d]	ΔH[e]	ΔG_{sol}	ΔG_{sln}
I	0	0	0	0	0	0	0	0
II‡	0.544	−1.652	−2.084	−0.566	−0.542	−1.375	3.100	2.558
III	−6.773	−0.281	0.218	0.981	−8.035	−6.574	6.780	−1.255
IV‡	−6.667	−0.554	−0.487	0.084	−7.087	−7.116	6.308	−0.780
V	−6.773	−0.205	0.169	0.585	−7.346	−6.618	5.440	−1.906
VI‡	−3.521	−0.718	−0.703	−0.162	−3.861	−4.168	4.070	0.209
VII	−12.191	−0.879	−0.339	1.378	−14.230	−12.503	5.845	−8.385
VIII‡	1.790	−1.214	−1.385	−0.615	1.408	−1.377	9.520	10.928
IX	−27.484	−2.697	−1.661	3.231	−33.195	−29.013	12.100	−21.095

[a] B3LYP/6-31+G**//HF/3-21+G* values in kilocalories per mole. The HF/3-21+G* frequencies were scaled by an empirical factor of 0.9135 to correct for errors in the potential energy surface. The solvation energies were calculated from the geometry optimized in the gas phase using the SCRF model implemented in Jaguar (25): the van der Waals radii of the 2′ oxygen and nonbridging oxygens of the phosphate group were fitted to reproduce the solvation energies of H_3PO_4, $H_2PO_4^-$, and HPO_4^{2-} (Leclerc et al., unpublished). [b] States marked with a double dagger symbol are transition states, and the other states are minima on the potential energy surface. [c] Zero-point-energy contribution. [d] $\Delta G_{gas} = \Delta E + \Delta ZPE + \Delta E_{TRV} + \Delta(PV) - T\Delta S_{TRV}$, where ΔE_{TRV} and ΔS_{TRV} include the translational, rotational, and vibrational contributions. ΔG_{sol} is the solvation free energy, and ΔG_{sln} is the total free energy difference in solution. The entropy (S_{vib}), zero-point energy (ZPE), and vibrational energy (E_{vib}) were calculated from the frequencies and geometries according to standard statistical mechanical formulas (26). The rotational (E_{rot}) and translational (E_{trans}) energies and the work term (PV) were treated classically; an ideal gas PV term was added to obtain the Gibbs free energy of the reaction. [e] The enthalpies of reaction were calculated as the sum of the energy difference with respect to the reactant and the thermal correction to enthalpy: $\Delta H = \Delta E + \Delta(PV)$. The calculated values for I are $E = -1981.758\ 766$ hartree, ZPE = 0.389 62 hartree, $\Delta(PV) = 0.420\ 251$ hartree, $E_{TRV} = 263.712$ kcal/mol, $\Delta S_{TRV} = 189.433$ cal/mol, and $\Delta G_{sol} = -1.15$ kcal/mol.

considered that the 2′ OH activation proceeds via a solvated metal hydroxide as proposed for a single-ion mechanism, but we do not exclude other possible modes of activation; see Figure 1), (2) nucleophilic attack on the phosphorus (Figure 3B), (3) a coordination change at the first metal site from a pentacoordinated magnesium to a hexacoordinated magnesium (Figure 3C), and (4) the departure of the leaving group (Figure 3D). There are nine stationary points (numbered from I to IX) of which four are transition states (II‡, IV‡, VI‡, and VIII‡) and three are chemical intermediates (III, V, and VII), in addition to the reactant (I) and product (IX). The critical geometric parameters of the stationary points are listed in Table 1, and the calculated energies and free energies (see the Supporting Information) are given in Table 2. In the reactant, the first metal ion is pentacoordinated and not hexacoordinated, as it was in the starting structure used for the optimization; one water molecule has moved during the optimization to become hydrogen bonded to the O4′ sugar oxygen so that it no longer belongs to the first coordination shell of the metal. Interestingly, this change in coordination leads to better stabilization of the in-line conformation for an O2′−P distance more than 2.0 Å (see the Supporting Information for details); that is, the switch from a hexacoordinated metal to a pentacoordinated metal at site I is associated with an increase of the O2′−P−O5′ angle from 140 to 162° (compare stationary points 0 and I in Table 1). The second metal site is unchanged from its initial conformation and corresponds to a hexacoordinated magnesium. Overall, the resulting reactant structure has an in-line conformation stabilized by the positions and coordinations of the two metals (Figure 3A). The pentacoordinated magnesium ion at site I includes two inner-sphere ligands from the ribozyme (the oxygen O2′ and the nonbridging oxygen pro-R of the phosphate group); the other three ligands are two water molecules and one hydroxide ion. In this trigonal bipyramidal arrangement, the 2′ oxygen and the two coordinated water molecules (Figure 3A) occupy the equatorial positions; the hydroxide ion and the pro-R oxygen occupy the apical positions of the bipyramid (Figure 3A). The proton from the 2′ OH is in the plane of the bipyramid (defined by the pro-R and O2′ oxygens, the metal, and the hydroxide ions) and easily abstracted by the hydroxide ion; the distance between the O2′ and hydroxide-ion oxygens (less than 2.6 Å) corresponds to a relatively short hydrogen bond (present in the reactant and transition state, see Table 1). Thus, the deprotonation of the 2′ OH occurs without any major change in the geometry of the reactant: only the O2′−P distance is slightly shortened from 2.80 (Figure 3A, I) to 2.77 Å (Figure 3A, III). The hexacoordinated Mg^{2+} at site II is approximately octahedral with six ligands (the pro-R and O5′ oxygens from the RNA and four water molecules).

The nucleophilic attack also does not involve any major geometrical change. Only the O2′−P distance changes significantly (from 2.77 Å in III to 2.17 Å in IV), and the activation energy is very low; it equals 0.11 kcal/mol at the B3LYP/6-31+G**//HF/3-21+G* level (Figure 3B). The activation energy for the reverse reaction between the second intermediate (V) and the corresponding transition state (IV‡) is the same (0.11 kcal/mol); the second intermediate (V) has a further shortening of the O2′−P distance to 1.92 Å. The transition state geometry is essentially a trigonal bipyramid, which is maintained until product formation.

The third step corresponds to a structural change between the nucleophilic attack and the departure of the leaving group. Its essential feature is the change of the metal coordination at the first metal site from pentacoordinated to hexacoordinated, which is required for the reaction to proceed (Figure 3C); that is, the intermediate with two hexacoordinated metals (VII) corresponds to a symmetric state where the 2′ and 5′ bridging oxygens (after nucleophile activation) interact equally as strongly with both metals (the O2′−P bond starts to form with the O2′−P distance changing from 1.916 Å in V to 1.783 Å in VII, while the P−O5′ bond starts breaking with the P−O5′ distance changing from 1.692 Å in V to 1.709 Å in VII). This change occurs via the migration of the water molecule hydrogen bonded to the O4′ oxygen into the first coordination shell of the metal at site I, so that it again is hexacoordinated (Table 1). The activation barrier for this step is 3.3 kcal/mol. It leads to the formation of a third intermediate (VII), which is more stable (by 4.9 kcal/mol) than the second intermediate (V) and has a reverse activation energy of 8.7 kcal/mol.

The fourth (final) step involves the departure of the leaving group (5′ oxygen methyl), which is protonated to form CH_3OH by proton transfer from one of the water molecules coordinated to the second metal; this water becomes an OH^- ligand. As in the first step of the reaction that also involves a proton transfer,

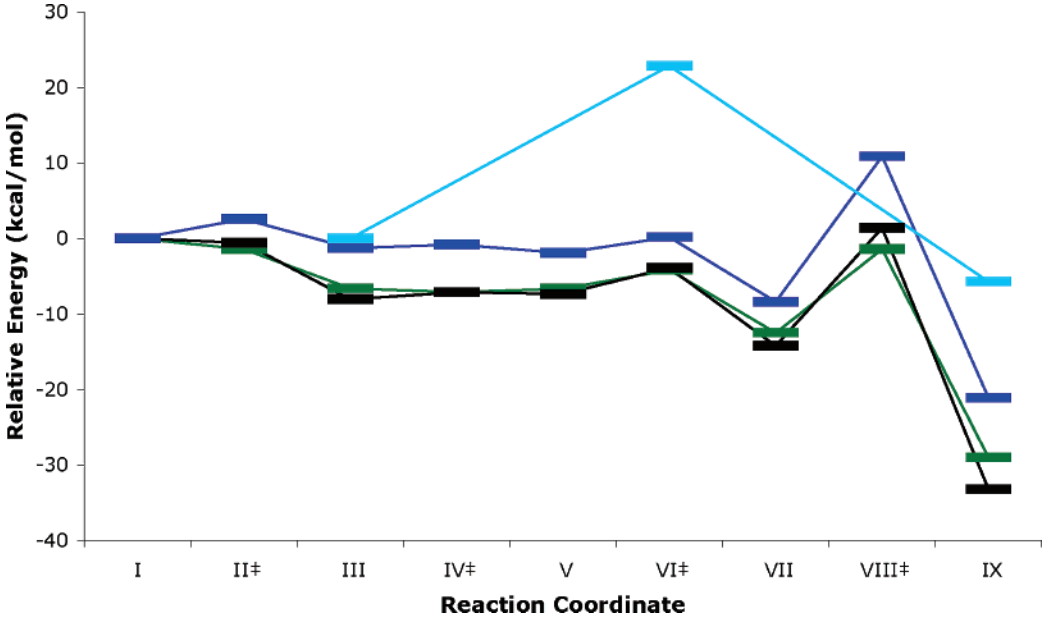

Figure 4. Reaction profiles of the proposed reaction mechanism. The energy profiles correspond to the total free energy difference (black line), the total free energy difference in solution (dark blue line), and the enthalpy difference (green line). For comparison, the energy profile corresponding to the total free energy difference in solution is also shown for a metal-free system (light blue line).

a short hydrogen bond is formed between the proton donor (one of the coordinated water molecules to the metal at site II) and the proton acceptor (the 5′ oxygen). However, the hydrogen bond is only formed in the transition state after the proton transfer has effectively occurred between the leaving group (CH_3O/Mg_{II}) and the water molecule (H_2O/Mg_{II}). The protonated leaving group (CH_3OH/Mg_{II}) is then dissociated from the 2′,3′ cyclic phosphate ribose but remains coordinated with the Mg^{2+} ion at site II (Figure 3D). This step has the highest forward activation energy (14.0 kcal/mol).

From the above description and the values in Table 2, the rate-limiting step for the overall reaction is the transition from the third intermediate (VII) to the product (IX) via the transition state (VIII‡). The calculated free energy barrier is $\Delta G^{\ddagger} = 19.3$ kcal/mol, which is close to the experimental value $\Delta G^{\ddagger} = 20.1$ kcal/mol. The measured value is for the overall reaction, but it has been suggested that the cleavage of the P−O5′ bond corresponds to the rate-limiting step for nonenzymatic and hammerhead-ribozyme-catalyzed reactions,[27,44] as found here. The calculated values for the activation energies ($\Delta H^{\ddagger} = 13.9$ kcal/mol, $E_a = 14.0$ kcal/mol) are in reasonable agreement with the experimental values ($\Delta H^{\ddagger} = 17.7$ kcal/mol, $E_a = 18.3$ kcal/mol). Since the activation free energies of the first three steps are all quite low (Table 2), the reaction could appear to be essentially concerted.

3.2. Energetics and Solvent Effects. The relative energies of all of the stationary points, with respect to the reactant as a reference, are listed in Table 2; the relative free energies both in the gas phase and in solution are also included. The calculations at the Hartree−Fock and Becke3LYP levels give similar energy profiles for the activation barriers; the rate-limiting step corresponds to the departure of the leaving group (see above and Figure 3D). In the calculations at the higher level of theory (B3LYP/6-31+G**//HF/3-21+G*), the energy barriers for the other steps are very small, the value is near zero for the nucleophilic attack ($\Delta\Delta G_{sln}^{III\rightarrow IV^{\ddagger}} = 0.47$ kcal/mol). The enthalpy makes the larger relative contribution to the free energy change in most of the reaction steps (Table 2 and Figure 4). The entropy represents between 19 and 45% of the free energy difference except for the stationary points V and VI‡, which correspond to the migration of the water molecule in the second reaction step (Figure 3C), for which the entropic component is more than 60% (97 and 64%, respectively). The free energy barriers of the reaction are larger than the activation barriers due to the entropic penalty (except for the formation of VII and IX). In solution, the free energy barriers are slightly lowered except for the departure of the leaving group where the barrier increases from 15.6 to 19.3 kcal/mol (Figure 4). The solvation free energy difference is large in the first step between the reactant and the first intermediate (6.78 kcal/mol between I and III, see Table 2) because the deprotonation of the 2′ OH required for the nucleophile activation involves a switch from a monoanion (−1) to a dianion (−2) of the RNA moiety (from I to III, Figure 3A), although the overall charge of the system does not change. By contrast, the differential solvent effect is small in the second and third steps of the reaction (the variation of solvation free energy is 2.7 kcal/mol or less between II‡ and VII‡) because the redistribution of charge is much smaller for the various stationary points with a trigonal bipyramidal geometry. In the last step, there is a second significant solvent effect that is related to two different events: the separation of charge between the partially dissociated products (the ribose 2′,3′ cyclic phosphate and the CH_3OH) and the delocalization of the hydroxide-ion charge formed after neutralization of the leaving group (CH_3OH). The redistribution of charge associated with the product formation is attenuated by the neutralization of the leaving group (from CH_3O^- to CH_3OH) via the proton transfer from a water molecule coordinated to the metal at site II (Figure 3D); the solvation free energy associated with this event is 3.7 kcal/mol (between VII and VIII‡, see Table 2). The delocalization of the hydroxide-ion charge onto three water molecules involves secondary proton transfers (two water molecules coordinated to the metal at site II and one water molecule coordinated to the metal at site I, see Figure 3D). The solvation free energy associated with this event is 2.6 kcal/mol. Nevertheless, the magnitude of the solvent effects is much smaller than that found, for example, in the nonenzymatic ionic ester hydrolysis. There, the solvation free energy change between the reactant and products is estimated to be 49.4 kcal/mol (Supporting Information Figure S2) versus 12.1 kcal/mol

TABLE 3: Interaction Energies between Donor and Acceptor Orbitals from the NBO Analysis[a]

vicinal interactions	reactant I	TS1 II‡	intermediate 1 III	TS2 IV‡	intermediate 2 V	TS3 VI‡	intermediate 3 VII	TS4 VIII‡	product IX
$n_{O^-(Mg(I))} \rightarrow \sigma^*_{O2'-H}$ [b]	47.4	105							
$n^*_{Mg(I)} \rightarrow \sigma_{O2'-H}$	4.80	6.40							
$n^*_{Mg(I)} \rightarrow \sigma_{O2'-H}$	1.96	4.60							
$n_{O2'} \rightarrow \sigma^*_{P-O5'}$	1.0	0.98	4.6	5.4	4.4	5.2	5.7		
$n_{O5'} \rightarrow \sigma^*_{P-O2'}$					5.2	5.3	5.9	32.4	0.48
$\sigma_{P-O2'} \rightarrow \sigma^*_{P-O5'}$					26.4	28.0	30.3		
$\sigma_{P-O5'} \rightarrow \sigma^*_{P-O2'}$					32.6	30.6	31.7		
$\sigma^*_{P-O2'} \rightarrow \sigma^*_{P-O5'}$					164	231	502		
$n_{O_2'} \rightarrow n^*_{Mg(I)}$	19.2	21.3	42.3	37.5	28.3	25.7	26.4	24.1	2.88
$n_{O_R} \rightarrow n^*_{Mg(I)}$	25.3	25.5	20.6	20.5	24.2	26.1	24.2	28.1	25.3
$E_{orbital} = \sum\{n_{O_{RNA}} \rightarrow n^*_{Mg(I)}\}$ [c]	44.5	46.8	62.9	58.0	52.5	51.8	50.6	52.2	28.2
$E_{orbital} = \sum\{n_{Oi} \rightarrow n^*_{Mg(I)}\}$ [d]	138	136	142	138	133	131	155	160	138
$n_{O_5'} \rightarrow n^*_{Mg(II)}$ [e]	13.5	13.3	16.4	23.4	22.5	25.8	26.7	13.0	24.8
$n_{O_R} \rightarrow n^*_{Mg(II)}$	27.6	27.8	26.7	26.6	28.7	31.2	28.3	27.9	23.2
$E_{orbital} = \sum\{n_{O_{RNA}} \rightarrow n^*_{Mg(II)}\}$	41.1	41.1	43.1	50.0	51.2	57.0	55.0	40.9	48.0
$E_{orbital} = \sum\{n_{Oi} \rightarrow n^*_{Mg(II)}\}$	145	145	148	154	155	156	154	154	153

[a] B3LYP/6-31+G(d,p)//HF/3-21+G* values in kilocalories per mole. [b] Mg(I) refers to metal at site I. [c] The energy value corresponds to the sum of the second-order perturbative estimates of the stabilization energies between donor−acceptor pairs where $n_{O_{RNA}}$ refers to the donor p lone pairs of the oxygen atoms belonging to the RNA moiety (pro-R and 2′ oxygen atoms at site I and pro-R and 5′ oxygen atoms at site II). [d] Same as footnote *c* except that n_{Oi} refers to the donor p lone pairs of the oxygen atoms from all ligands (RNA and water molecules). [e] Mg(II) refers to metal at site II.

for the present system. The total free energy change including the solvation contribution is then −21 kcal/mol (see Table 2). However, it should be noted that the geometries of the reactant and product are likely not fully relaxed in the catalytic pocket of the hammerhead ribozyme, as they are in this model system. Intramolecular interactions can make the reactant more stable or more likely in this case the product less stable and thus reduce the relative energy difference between the reactant and product. Such relative stabilization to equalize the reactant and product free energy has been found in many enzymes (e.g., triose phosphate isomerase) and could explain the observed reversibility of the reaction.[45]

3.3. Natural Orbital Analysis. One approach to analyze the electronic changes taking place during the reaction is to look at the behavior of natural bond orbitals (NBOs) which are commonly used to describe hybridization and covalency effects in molecules. They are localized on a small number of atoms and describe the Lewis-like molecular bonding pattern of electron pairs. The NBO analyses at the Becke3LYP/6-31+G**//HF-3-21+G* level show that the natural bond orbitals are different for the various steps of the reaction. We focus on three natural bond orbitals between (1) the 2′ oxygen and its proton before the O2′ H activation in the first step of the reaction ($\sigma_{O2'-H}$, I and II), (2) the phosphorus and the leaving group in the first three steps of the reaction ($\sigma_{P-O5'}$, I to VII), and (3) the phosphorus and the nucleophile in the last step of the reaction ($\sigma_{P-O2'}$, VII to IX). The $\sigma_{O2'-H}$ natural bond orbital is mostly localized on the 2′ oxygen with 83−86% (I to II) of the orbital consisting of basis functions on oxygen. The inner-sphere coordination to the hydroxide−metal complex strongly weakens the O2′−H bond ($n_{O^-(Mg(I))} \rightarrow \sigma^*_{O2'-H}$ from 47.4 kcal/mol for I to 105 kcal/mol for II, Table 3) and slightly increases the O2′−H polarization (in the triester-like mechanism, the contribution from the 2′ oxygen to $\sigma_{O2'-H}$ is less than 80% in the reactant that also involves a short hydrogen bond between the O2′ and the pro-Rp oxygen, Leclerc et al., to be published). The $\sigma_{P-O5'}$ natural bond orbital is mostly localized on the 5′ oxygen with 85−87% (I to VII) of the orbital consisting of basis functions on oxygen. In $\sigma_{P-O2'}$, the contributions from the phosphorus and oxygen to the $\sigma_{P-O2'}$ in V are 9 and 91%, respectively, and they end up at 15 and 85%, respectively, in the product (IX). The trigonal bipyramidal intermediates (V and VII) as well as the transition state that connects them (VI‡) both exhibit the natural bond orbitals $\sigma_{P-O2'}$ and $\sigma_{P-O5'}$. During the migration of the water molecule (associated with the coordination change of the metal at site I), the delocalization of the lone pair on the nucleophile into the P−O5′ antibonding orbital, which was present in the two first steps (nucleophile activation and nucleophilic attack), remains with an increasing interaction energy and contributes to weaken the P−O5′ bond ($n_{O2'} \rightarrow \sigma^*_{P-O5'}$ from 4.4 kcal/mol for V to 5.7 kcal/mol for VII). The three stationary points involved in this process (V to VII) are the only ones where the two natural bonds $\sigma_{P-O5'}$ and $\sigma_{P-O2'}$ are present at the same time; they also exhibit the presence of two specific non-Lewis NBOs ($\sigma_{P-O2'} \rightarrow \sigma^*_{P-O5'}$ and $\sigma^*_{P-O2'} \rightarrow \sigma^*_{P-O5'}$, see Table 3). The increasing σ-interactions into the P−O5′ antibonding orbital associated with the coordination change of the metal at site I contribute to weakening of the P−O5′ bond involved in the departure of the leaving group (P−O5′ bond going from 1.692 Å for V to 1.709 Å for VII, Table 1).

3.4. Reaction Path and Role of Metal Ions. The reaction path was followed by performing intrinsic reaction coordinate (IRC) calculations,[46] showing that the transition states connect the corresponding reactant, product, and intermediates (Supporting Information Figure S3). In the presence of metal ions, the reaction is sequential according to the model developed here, although, as pointed out above, the kinetics might appear concerted due to the small activation free energies for several of the early steps. There is no direct spectroscopic evidence for the existence of chemical intermediates, but the hammerhead-ribozyme kinetics have been interpreted as suggesting that an intermediate exists;[47] see also earlier ab initio molecular orbital calculations on phosphates and phosphoranes.[25] Interestingly, the model developed for the metal-free reaction suggests a concerted mechanism where the nucleophilic attack and the departure of the leaving group are coupled (Leclerc et al., to be published separately). A comparison of the energy profiles in solution between the metal-assisted reaction and the metal-free reaction shows that metals contribute significantly to lowering

TABLE 4: Natural Energy Decomposition Analyses (NEDA) of the RNA−Metal Complexes[a]

	total binding energy					
molecule	ΔE_{tot}[b]	ES	POL	CT	EX	DEF
I	−311	−382	−242	−256	−43.9	614
II‡	−324	−405	−253	−315	−47.5	696
III	−644	−667	−332	−230	−43.3	628
IV‡	−644	−674	−327	−232	−43.5	633
V	−646	−681	−322	−233	−43.6	634
VI‡	−652	−689	−340	−234	−45.3	656
VII	−646	−683	−337	−257	−46.5	676
VIII‡	−307	−375	−236	−259	−42.6	606
IX	−379	−436	−269	−235	−44.9	607

[a] RHF/6-31+G**//RHF/3-21+G* values in kilocalories per mole. The calculations are based on the decomposition into three molecular fragments corresponding to the RNA model and the two hydrated metal ions treated with their solvation shell. [b] The binding energy for bringing together the three molecular fragments is given by ΔE_{tot} = ES + POL + CT + EX + DEF, sum of the electrostatic (ES), polarization (POL), charge transfer (CT), exchange (EX), and deformation (DEF) contributions calculated by the NBO 5.0 program.[47] The metal ion at site I is pentacoordinated from I to IV and hexcoordinated from V to VII. The metal ion at site II is hexacoordinated and includes the water molecule in the second solvation shell (I to IV) which is then transferred to the metal at site I (V to VII).

of the energy barriers; the overall free energy barrier is reduced by 12.0 kcal/mol (Figure 4).

Natural Energy Decomposition. To obtain a more detailed understanding of the influence of the metal ions on the different steps of the reaction, natural energy decomposition analyses (NEDA)[48] were performed for the stationary points. On the basis of this analysis, the binding energy between the RNA model and the two hydrated metals and its variation along the reaction coordinate were determined (Table 4). The binding energy was decomposed into two-body interactions between pairs of fragments—RNA−Mg_I, RNA−Mg_{II}, and Mg_I−Mg_{II} (Table 5)—and a non-pairwise-additive three-body interaction (Supporting Information Table S1), which are further decomposed into different energetic contributions. The method and details of the results of the NEDA are described in the Supporting Information.

Although the binding energy corresponding to the process of bringing together the RNA and the two hydrated metals is always favorable (RNA−Mg_I and RNA−Mg_{II} are favorable, while Mg_I−Mg_{II} is unfavorable), it varies significantly in the two steps of the reaction corresponding to changes of charge on the RNA moiety, that is, during the nucleophile activation (first step: I to III) and during the departure of the leaving group (fourth step), which involve a switch from a monoanionic RNA species to a dianionic RNA species and vice versa (Figure 5). In the first step of the reaction (I to III, Figure 3A), there is a large increase (of more than 100%) in binding energy (>300 kcal/mol) associated with the monoanion-to-dianion conversion due to the 2′ OH deprotonation which occurs late along the reaction pathway (Supporting Information Figure S3A). As expected, the RNA−Mg_I interaction that involves a direct coordination between the 2′ oxygen and Mg_I represents the major contribution to the increased binding energy. However, the RNA−Mg_{II} interaction contributes about one-third of the increase (Table 5). In the reactant (I), the RNA−Mg_{II} interaction represents the major contribution to the total binding energy: 43% versus 32% for the RNA−Mg_I interaction. After formation of the first intermediate (III), the relative contributions of the RNA−Mg_{II} and RNA−Mg_I interactions are reversed (34% versus 43%) and the RNA−Mg_I interaction becomes predominant in the total binding energy (Figure 5A).

From the first intermediate to the product, the RNA−Mg_I interaction decreases while the RNA−Mg_{II} interaction increases. The two-body interaction term between the hydrated metals (Mg_I−Mg_{II}) remains essentially constant; it is destabilizing due to the metal−metal electrostatic repulsion (Table 5). The changes in the two RNA−metal terms (RNA−Mg_I and RNA−Mg_{II}) are compensatory and partly associated with the migration of the water molecule from the second solvation shell of Mg_{II} to the first solvation shell of Mg_I. The RNA−metal complex is destabilized by the three-body term which arises mainly from the polarization term that represents up to 74% of the unfavorable contribution (Supporting Information Table S1). The two dominant contributions are the electrostatic (ES) and deformation (DEF) terms; each term contributes about 35%. The ES term is favorable while the DEF term is unfavorable to the association of the RNA with the metals. The DEF term is predominantly associated with the Pauli repulsion that prevents the charge distribution of the RNA fragment from penetrating that of the hydrated metal fragments and vice versa. The polarization (POL) and charge transfer (CT) terms are the two other favorable terms that contribute significantly to the binding energy: POL contributes from 16 to 18% and CT from 12 to 17%. The exchange (EX) term represents only 2−3% of the binding energy. The decreasing ES and POL components for RNA−Mg_I and the increasing ES and POL components for RNA−Mg_{II} explain the compensation in the binding between these two pairs of fragments (Table 5). The stabilization energy comes in part from the delocalization of the lone pairs on the 2′ and 5′ oxygens into the metal orbitals (nonbonding lone pairs)

TABLE 5: Natural Energy Decomposition Analyses (NEDA) of the Two-Body Interactions[a]

	two-body term (RNA + Mg)[b]						two-body term (Mg + Mg)					
molecule	Δ*E*(I/II)	ES(I/II)	POL(I/II)	CT(I/II)	EX(I/II)	DEF(I/II)	Δ*E*	ES	POL	CT	EX	DEF
I	−202/−267	−247/−284	−119/−121	−128/−101	−23.5/−18.2	315/258	152	149	−20.8	−30.1	−3.92	57.8
II‡	−213/−267	−269/−286	−127/−122	−185/−103	−27.2/−18.5	395/262	153	150	−20.5	−28.6	−3.74	55.1
III	−520/−404	−510/−418	−216/−135	−108/−116	−22.9/−19.2	336/285	257	261	−19.4	−18.9	−2.13	37.0
IV‡	−504/−423	−500/−438	−196/−153	−109/−117	−21.6/−20.9	322/305	259	263	−19.6	−19.3	−2.12	37.4
V	−496/−436	−495/−450	−184/−163	−113/−116	−21.0/−22.0	316/316	261	265	−19.6	−18.4	−2.03	36.0
VI‡	−498/−441	−497/−461	−183/−173	−110/−123	−20.8/−24.0	313/340	263	269	−20.6	−16.4	−1.79	32.8
VII	−466/−469	−478/−476	−180/−171	−139/−121	−24.8/−21.3	355/320	266	271	−18.8	−13.6	−1.77	29.5
VIII‡	−287/−164	−296/−212	−145/−95.0	−110/−138	−20.4/−21.2	284/303	131	133	−16.1	−18.1	−2.10	34.5
IX	−137/−280	−159/−279	−69.7/−128	−77.3/−93.0	−14.0/−16.5	183/235	25.4	2.00	−84.3	−52.0	−14.3	174

[a] RHF/6-31+RHF/6-31+G*//RHF/3-21+G* values in kilocalories per mole. The binding energy calculated as previously (Table 3) is decomposed into two-body interactions between pairs of fragments (RNA + Mg_I, RNA + Mg_{II}, and Mg_I + Mg_{II}) and a non-pairwise-additive three-body term (Table 5, Supporting Information). [b] For comparison, the binding energies of the two (RNA + Mg) pairs, corresponding to the metal sites I and II, respectively, are given together separated by a slash.

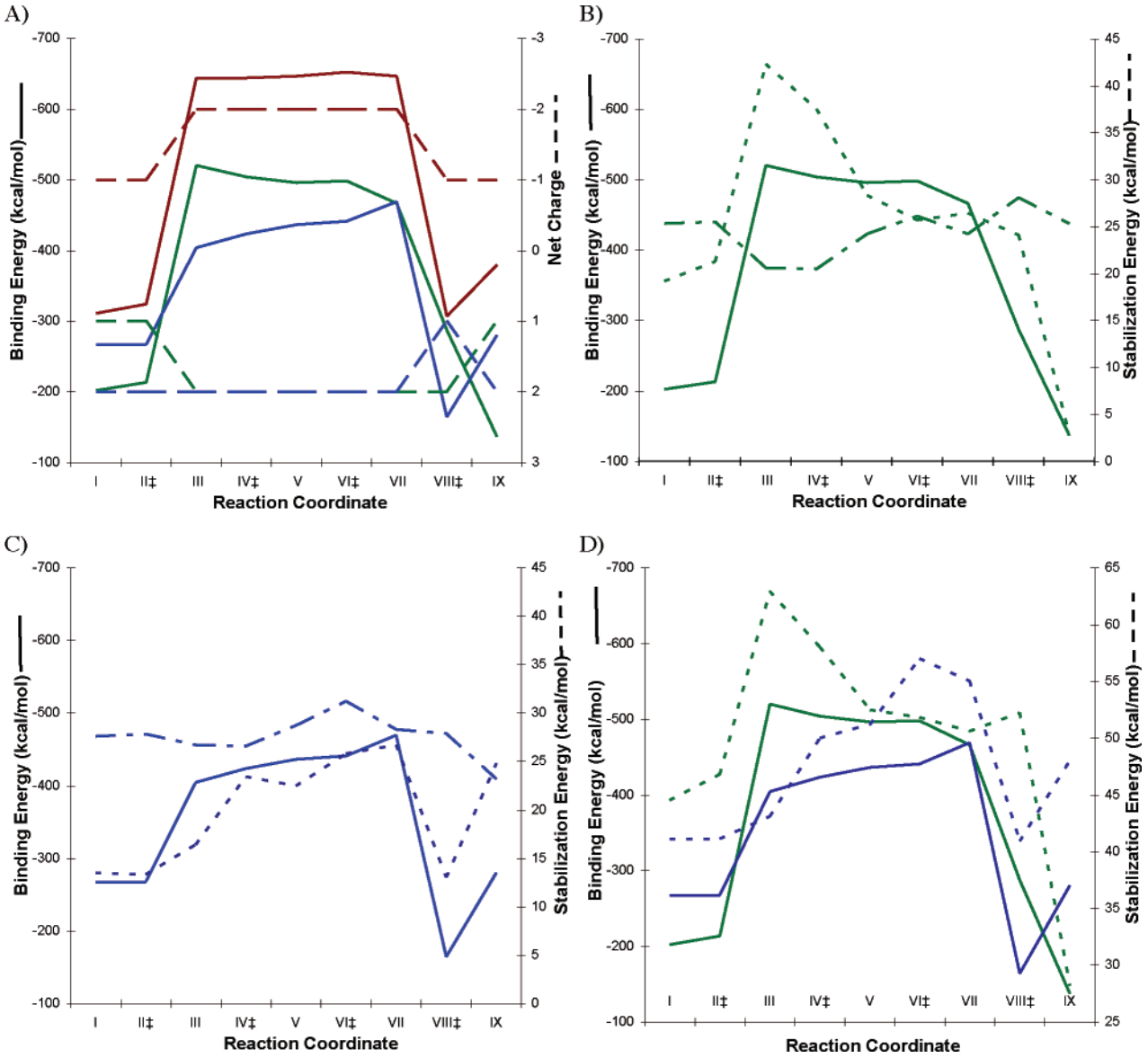

Figure 5. Binding energy along the reaction pathway of the RNA−metal complex and comparison with the stabilization energy from the delocalization of the lone pairs on the bridging oxygens into the metal orbitals. (A) The binding energy (left-hand vertical axis), calculated at the HF/6-31+G**// HF/3-21+G* level by NEDA, corresponds to the energy to bring together three fragments: the RNA moiety and each of the two hydrated metal ions (metal and solvation shells). The total binding energy between the three fragments (solid red line) and the relative contribution (two-body interactions) from the metal at site I (RNA−Mg_I, solid green line) and the metal at site II (RNA−Mg_{II}, solid blue line) interacting with the RNA moiety are shown. The dashed lines (right-hand vertical axis) indicate the net charge on the RNA moiety (dashed red line), on the hydrated metal at site I (dashed green line), and on the hydrated metal at site II (dashed blue line). (B) The contribution from the RNA−Mg_I interaction (solid green line) is compared with the stabilization energy (indicated as positive on the right-hand axis) from the delocalization of the lone pairs on the pro-R and 2′ oxygen into the metal I orbitals ($n_{O_R} \rightarrow n^*_{Mg_I}$, dashed−dotted line; $n_{O2'} \rightarrow n^*_{Mg_I}$, dotted green line). (C) The contribution from RNA−Mg_{II} interaction is compared with the stabilization energy from the delocalization of the lone pairs on the pro-R and 5′ oxygen into the metal II orbitals ($n_{O_R} \rightarrow n^*_{Mg_{II}}$, dashed−dotted blue line; $n_{O5'} \rightarrow n^*_{Mg_{II}}$, dotted blue line). (D) The contributions from the RNA−Mg_I and RNA−Mg_{II} interactions (solid green and blue lines) are compared with the total stabilization energy from the delocalization of both the lone pairs on the pro-R and 2′ oxygen into the metal I orbitals (dotted green line) or from the delocalization of both the lone pairs on the pro-R and 5′ oxygen into the metal II orbitals (dotted blue line). In parts B−D, the orbital delocalization contributions correspond to the right-hand vertical axis.

at Mg_I and Mg_{II} ($n_{O2'} \rightarrow n^*_{Mg_I}$ and $n_{O5'} \rightarrow n^*_{Mg_{II}}$) that represents covalency contributions to the RNA−metal interactions (Figure 5B and C).

Natural Orbital Analysis. As mentioned before, the coordination of the 2′ oxygen to Mg_I contributes to weaken the O2′−H bond in the first step of the reaction. The destabilization due to the delocalization of the antibonding orbitals of metal-ion lone pairs of Mg_I into the antibonding σ orbital of the O2′−H bond increases ($n^*_{Mg(I)} \rightarrow \sigma^*_{O2'-H}$ from 1.96 kcal/mol for I to 4.60 kcal/mol for II), while the corresponding stabilization due to the delocalization of the antibonding orbitals of metal-ion lone pairs of Mg_I into the bonding σ orbital of the O2′−H bond increases but to a lesser extent ($n^*_{Mg(I)} \rightarrow \sigma_{O2'-H}$ from 4.80 kcal/mol for I to 6.40 kcal/mol for II, Table 3). The net destabilization effect of the metal Mg_I on the O2′−H bond is thus 1.8 kcal/mol.

From the first intermediate to the product, the stabilization energy due to the delocalization of the lone pair on the 2′ oxygen, corresponding to the coordination to Mg_I, decreases ($n_{O2'} \rightarrow n^*_{Mg_I}$ from 42 to 2.9 kcal/mol). Simultaneously, the stabilization energy due to the delocalization of the lone pair on the 5′ oxygen corresponding to the coordination to Mg_{II}

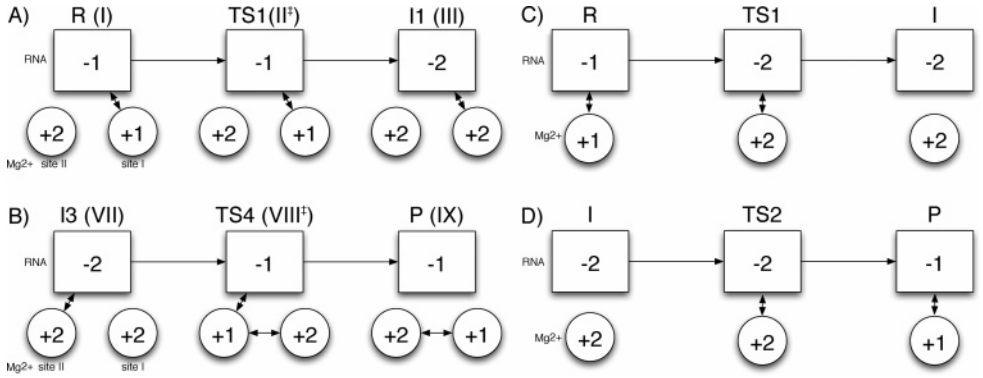

Figure 6. Changes of charge distribution between the RNA and hydrated metal moieties along the reaction pathway in the steps involving the monoanion/dianion interconversions for the current two-metal-ion model (A and B) and the single-metal-ion model (C and D, Torres et al., 2003). (A) Monoanion/dianion conversion in the first step of the reaction. The three corresponding stationary points I, II‡, and III are represented in a schematic way. (B) Dianion/monoanion conversion in the last and rate-determining step of the reaction. The three corresponding stationary points VII, VIII‡, and IX are represented similarly. (C) Monoanion/dianion conversion in the first step of the reaction. (D) Dianion/monoanion conversion in the last and rate-determining step of the reaction. The rectangle represents the RNA moiety, and the spheres represent the hydrated metal moieties (sites I and II are labeled as in Figure 3, and the fragment moieties are defined as in the NEDA calculations). The single arrows indicate the forward direction of the reaction. The double arrows indicate the moieties involved in the changes of charge distribution.

increases somewhat ($n_{O5'} \rightarrow n^*_{Mg_{II}}$ from 16 kcal/mol for III to 25 kcal/mol for IX). As the O2′−P bond forms, the delocalization of the lone pair on the 2′ oxygen into the antibonding orbitals of metal-ion lone pairs of Mg_I decreases (Figure 5B). Inversely, as the P−O5′ bond breaks, the delocalization of the lone pair on the 5′ oxygen into the antibonding orbitals of metal-ion lone pairs of Mg_{II} increases (Figure 5C). We can define a covalency contribution to RNA−metal binding as the sum of the stabilization energies associated with the delocalization of the lone pairs on all of the RNA oxygens into the antibonding orbitals of metal-ion lone pairs of Mg_I and Mg_{II}. It includes the contribution from the 2′ and pro-R oxygens interacting with Mg_I ($n_{O2'} \rightarrow n^*_{Mg_I}$ and $n_{O_R} \rightarrow n^*_{Mg_I}$) and that from the 5′ and pro-R oxygens interacting with Mg_{II} ($n_{O5'} \rightarrow n^*_{Mg_{II}}$ and $n_{O_R} \rightarrow n^*_{Mg_{II}}$). Thus, there is a correlation between the RNA−metal binding energy (calculated with the NEDA) and the covalency contribution to RNA−metal binding; the major covalency contributions come from the delocalization of the lone pair on the 2′ and 5′ oxygens into the antibonding orbitals of metal-ion lone pairs of Mg_I and Mg_{II}, respectively (Figure 5B−D). The contributions from the delocalization of the lone pair on the pro-R oxygen into the antibonding orbitals of both metals have small variations along the reaction path (Figure 5B and C). The total stabilization energy for σ-interactions that transfer charge from occupied lone-pair natural bond orbitals on the oxygen atoms, belonging to both RNA and water molecules, into empty non-Lewis orbitals on the metal ions ($E_{orbital} = \sum\{n_{Oi} \rightarrow n^*_{Mg(I)}\}$ and $E_{orbital} = \sum\{n_{Oi} \rightarrow n^*_{Mg(II)}\}$, Table 3) varies to a lesser extent than the stabilization energy corresponding to the covalency contribution to RNA−metal binding. Indeed, the decreasing stabilization energy from III to IX for the σ-interactions in Mg_I−O2′ and the increasing stabilization energy from I to VII for the σ-interactions in Mg_{II}−O5′ are compensated by increasing and decreasing the stabilization energies, respectively, arising from water ligands (Table 3). The total stabilization energy for the σ-interactions in metal−oxygen bonds is greater in the case of the hexacoordinated metal Mg_{II} (I to VI), but the difference with the pentacoordinated metal Mg_I can be small (142 kcal/mol versus 148 kcal/mol in III, Table 3) because of the stronger covalency contribution to RNA−Mg_I binding in comparison with RNA−Mg_{II} binding (62.9 kcal/mol versus 43.1 kcal/mol in III, Table 3). Nevertheless, the noncovalency contributions to RNA−metal binding, especially the electrostatic contribution, are more important than the covalency contributions.

During the last step of the reaction, the total binding energy drops by more than 40% in going from the 3rd intermediate (VII) to the product (IX) when the 5′ oxygen is protonated and the proton of a water molecule coordinated to Mg_{II} is transferred to the leaving group (Table 4). This large change in binding energy is again associated with a modification of the net charge on the RNA moiety (a dianion-to-monoanion conversion in this case) that arises from the partial separation of the leaving group from the ribose 2′,3′ cyclic phosphate (Figure 5A). The destabilization of the RNA−metal complex is mainly electrostatic (the ES and POL contributions decrease), and it is only partly compensated by the decrease in the unfavorable two-body term Mg_I−Mg_{II}, which is reduced by 90% (Table 4) and by the three-body term which also becomes less destabilizing (Supporting Information Table S1). This destabilization is even more pronounced in the last transition state (VIII‡) than in the product (IX) and is associated with a double change in the charge distribution from the third intermediate (VII) to the fourth transition state (VIII‡) to the product (IX). The first change in the charge distribution is due to the first proton transfer from a coordinated water molecule to the 5′ oxygen which occurs early in the reaction pathway, while the second one is due to the second proton transfer between two water molecules each coordinated to one of the metal ions (Supporting Information Figure S3D).

Monoanion/Dianion Interconversions. The two steps of the reaction that involve a change in the net charge on the RNA moiety, that is, the nucleophile activation of the 2′ oxygen (first step) and the departure of the leaving group (last step), correspond to a monoanion/dianion conversion (first step) and a reverse dianion/monoanion conversion (last step); that is, the net charge on the RNA moiety switches from −1 (I) to −2 (III) in the first step and back from −2 (VII) to −1 (IX) in the last steps (Figure 6). As the calculations have shown, the free energy barrier is low in the first step ($\Delta\Delta G_{sln}^{I \rightarrow II‡} = 2.56$ kcal/mol) while it is high in the last step ($\Delta\Delta G_{sln}^{VII \rightarrow VIII‡} = 19.3$ kcal/mol). Both reactions lead to a lowering of the energy ($\Delta\Delta E$) and free energy ($\Delta\Delta G_{sln}$) of the system, as expected. Whether there is a low activation energy (as in the first reaction) or a high activation energy (as in the last reaction) depends on

whether the stabilizing interactions appear as the system goes from the reactant to the transition state or from the transition state to the product, respectively.

The two steps both involve proton transfers between the RNA moiety and a hydrated metal: in the first step, the proton transfer is the only chemical process and it occurs late along the reaction pathway (i.e., after the transition state), while the proton transfer occurs early in the last step (i.e., before the transition state) and is concurrent with the P−O5′ bond breaking. The chemical process which corresponds to the higher energy barrier during the two first steps of the reaction is the proton transfer ($\Delta\Delta G_{sln}^{I\rightarrow II^{\ddagger}} = 2.56$ kcal/mol) and not the nucleophilic attack ($\Delta\Delta G_{sln}^{III\rightarrow IV^{\ddagger}} = 0.48$ kcal/mol). In the first step, the existence of a low barrier transition state for the proton transfer ($\Delta E = 0.544$ kcal/mol, $\Delta G_{gas} = -0.542$ kcal/mol, $\Delta G_{sol} = 3.1$ kcal/mol, see Table 2) is consistent with the results from a quantum chemical study on the proton transfer in RNase A catalysis involving the formation of short, strong hydrogen bonds ($\Delta E = 1.07$ kcal/mol, $\Delta G_{gas} = -1.24$ kcal/mol, 2.85 kcal/mol $\leq \Delta G_{sol} \leq$ 3.89 kcal/mol[49]). This low barrier for proton transfer is also in agreement with the explanation proposed for rapid enzyme-catalyzed proton abstraction associated with late transition states.[50] In the particular case of phosphodiesters, the low barrier for proton transfer in the reaction catalyzed by RNase A was also explained by the stabilization of the developing negative charge in the transition state that reduces the structural reorganization between the reactant and the transition state.[51] In this two-metal-ion model, the difference in the magnitude of the energy barriers for the two monoanion/dianion interconversions lies in the synchronization (or lack thereof) between the actual proton transfers and the associated molecular processes. In general, it is expected that a product stabilizing factor that lags behind bonding changes or the loss of a reactant stabilizing factor that is ahead of bonding changes enhances the barrier. By contrast, the late loss of a reactant stabilizing factor or the early development of a product stabilizing factor would lower the barrier.

In the first step, there is only one chemical process (cleavage of the 2′ O−H bond) that corresponds to the proton transfer associated with the nucleophile activation and a single change of charge distribution between the three fragments of the complex: the RNA moiety, the hydrated metal at site I, and the hydrated metal at site II (between $II^{\ddagger}$ and III, Figure 6A). The proton transfer occurs late along the reaction pathway (Supporting Information Figure S3A), so that the reactant I and the transition state $II^{\ddagger}$ are very close in structure (Table 1 and Figure 3A) and in energy ($\Delta\Delta G_{gas}^{I\rightarrow II^{\ddagger}} = -0.54$ kcal/mol, Table 2) and conserve the same net charge of −1 on the RNA moiety (monoanion). This similarity between the reactant I and the first transition state $II^{\ddagger}$ is typical for a late loss of reactant stabilizing factors that leads to a low intrinsic barrier (the cleavage of the 2′ O−H bond occurs after the transition state).

The last step of the reaction is considerably more complex than the first, since there are several concurrent chemical processes. The proton transfer to the 5′ oxygen of the leaving group is associated with the first change of the charge distribution, and there is the breaking of the P−O5′ bond and a second proton transfer between the two hydrated metals, where the negative charge (OH^-) formed on the metal coordinated to the leaving group is transferred from Mg_{II} in $VIII^{\ddagger}$ to Mg_I in IX (Figure 6B). The main process, corresponding to the P−O5′ bond breaking, occurs rather late along the reaction pathway, while the first proton transfer occurs prior to the transition state (Supporting Information Figure S3D). The imbalance of the transition state is reinforced by the poor synchronization between each of the two chemical processes and the concurrent molecular processes corresponding to the charge delocalization and solvation. The first proton transfer corresponding to the change of net charge on the RNA moiety between the reactant (dianion VII) and the transition state (monoanion $VIII^{\ddagger}$) is characterized by an unfavorable electrostatic contribution to the RNA−metal interaction ($\Delta\Delta E_{ES}^{VII\rightarrow VIII^{\ddagger}} = 308$ kcal/mol, Table 4). On the other hand, the late second proton transfer induces a charge delocalization between the two hydrated metals that corresponds to an electrostatic stabilizing factor ($\Delta\Delta E_{ES}^{VIII^{\ddagger}\rightarrow IX} = -61$ kcal/mol, Table 4). This product stabilization is developed late along the reaction pathway, after the bond breaking at the TS (in the IRC profile: shoulder observed after the TS, Figure 5D). It can be assigned as an electrostatic contribution (noncovalency contribution) to the RNA−metal binding, which is less unfavorable for the product than for the transition state ($\Delta\Delta E_{ES}^{VII\rightarrow IX} =$ 247 kcal/mol vs $\Delta\Delta E_{ES}^{VII\rightarrow VIII^{\ddagger}} = 308$ kcal/mol). In summary, the high energy barrier of the rate-limiting step arises from the early destabilization of the third intermediate and the late stabilization of the product, associated with the P−O5′ bond breaking and the secondary proton transfers.

In the single-metal-ion model developed by Torres et al.,[20] there are two equivalent steps corresponding to monoanion/dianion interconversions (Figure 6C and D). Interestingly, the first transition state that corresponds to a monoanion-to-dianion conversion exhibits a high energy barrier (activation barrier of 18.6 kcal/mol). On the other hand, in the last step of the reaction, the second transition state corresponding to a reverse dianion-to-monoanion conversion exhibits a relative low energy barrier (relative activation barrier of 2.2 kcal/mol from the intermediate).[20] In the first step (Figure 6C), the proton transfer is early (and concurrent with the nucleophilic attack) and ahead of the transition state, while it is late in the last step of the reaction (Figure 6D) and lags behind the transition state. Although the energetic trend is opposite with respect to that of the two-metal-ion model, we can find common features between the two models (Figure 6). The comparison of the two models suggests that the monoanion/dianion interconversions induced by proton transfer exhibit (1) a high energy barrier when the charge redistribution is ahead of the transition state and (2) a low energy barrier when the charge redistribution lags behind the transition state. In the two-metal-ion model, the particularly low energy barrier involved in the monoanion-to-dianion conversion (first step) is associated with a proton transfer between two common metal ligands (O2′H and OH^- at site I) and thus only involves a very localized charge redistribution between the reactant and the first transition state ($II^{\ddagger}$).

3.5. Novelty of the Two-Metal-Ion Model. The two-metal-ion model described here is similar in spirit to the dianionic mechanism proposed by von Hippel et al.[26] However, the present work provides quantitative calculations of the mechanism which make possible a detailed understanding not available from the earlier, more qualitative description. The data supporting a two-metal-ion model[24−28] suggest that the metal ions act as Lewis acids (i.e., stabilizing the negative charge on the bridging 2′ and 5′ oxygens, Figure 1C) and not as general acids/bases, as was proposed for the single-metal-ion model (Figure 1B); the latter was inspired by the RNase A mechanism for transphosphorylation (Figure 1A). In the two-metal-ion model described here, the metal Mg_I which is coordinated to the 2′ oxygen acts as a Lewis acid by polarizing the 2′ O−H bond and thus facilitating the deprotonation. The calculated activation free energy barrier for the 2′ OH deprotonation and for the

nucleophilic attack is 2.6 kcal/mol. This contrasts with single-metal-ion-model estimates of 12 kcal/mol[52] and 18.6 kcal/mol.[20] The large energy difference is explained by the fact that, in the two-metal-ion model, the pK_a of the 2′ OH is lowered by the direct (inner-sphere) coordination of Mg_I to the 2′ oxygen, which polarizes the hydroxide bond, and that the dianion formed after the nucleophile activation is stabilized by both metals. These two features are absent from the single-metal-ion model. The NEDA results (see section 3.4) suggest that the stabilization of the RNA−metal complex, in which the RNA moiety is a dianion, is due both to Mg_I (2/3) and Mg_{II} (1/3). The presence of two metal ions not only makes the nucleophile activation more favorable, but it also stabilizes the RNA−metal complex in a conformation for in-line attack. As result, the free energy barrier in the solvated system for the second step of the reaction (the nucleophilic attack) is significantly lowered; it is 22.8 kcal/mol in the absence of the metal ions and 0.47 kcal/mol in their presence. The calculations performed with different geometries indicate that the pentacoordinated (rather than hexacoordinated) metal coordinated to the 2′ oxygen plays an important role in stabilizing the geometries which facilitate the two first steps of the reaction and contributes to lower their energy barriers (data not shown). However, the calculations indicate that the departure of the leaving group prefers a hexacoordinated state for both metals, so that a switch from Mg_I(V) to Mg_I(VI) takes place in the formation of the last intermediate. The NBO analyses show that the process of coordination change, associated with the natural bond orbitals $\sigma_{P-O2'}$ and $\sigma_{P-O5'}$, prepares the system for the departure of the leaving group. The increasing delocalization of the lone pair on the 2′ oxygen into the P−O5′ antibonding orbital, during the coordination change (V to VII), contributes to slightly weaken the P−O5′ bond before the departure of the leaving group. Product formation is facilitated by the delocalization of the hydroxide ion through secondary proton transfers involving two water molecules; the first one belongs to the solvation shell of Mg_{II} (in the axial position opposite the 5′ oxygen), and the second one belongs to the solvation shell of Mg_I (in the axial position opposite the 2′ oxygen). The proton transfer that occurs in the protonation of the 5′ oxygen in the rate-limiting step of the reaction is reminiscent of the single-metal-ion model (Figure 1B).

A theoretical model based on a single-metal-ion model and involving a similar proton transfer was proposed recently.[20] However, since the metal is not directly coordinated to the 5′ oxygen, it mostly behaves as a general acid/base. In the two-metal-ion model developed here, Mg_{II} acts both as a general acid and as a Lewis acid by giving a proton from one of its coordinated water molecules to the 5′ oxygen and accepting its electrons, a feature that has not been proposed in previous discussions of two-metal-ion models.[24−28,37,52] A two-metal-ion model was proposed by Boero et al. after this paper was completed, using a Car−Parrinello molecular dynamics (MD) simulation method for a model system.[53] In this model, the base generated by the spontaneous deprotonation of a water molecule located close to the 5′ leaving group is involved in the neutralization of the 5′ oxyanion. A similar neutralization occurs in the current model, but the water molecule involved is in the inner-sphere coordination of the metal at site II and the proton transfer precedes the P−O5′ bond breaking (Supporting Information Figure S3D). Both models follow a reaction path in which the nucleophile activation proceeds via a metal hydroxide as the general base, the subsequent nucleophilic attack leads to the formation of a trigonal bipyramidal structure, and the rate-limiting step is the departure of the leaving group. The major differences between the two models concern the interactions with the metal ions; that is, the metal solvation shells (metal/water or metal/OH−) and the metal coordinations with the RNA moiety differ at all steps of the reaction (in particular the coordinations with the nonbridging oxygens, Boero et al.,[53] Tateno, personal communication). As pointed out by Boero et al.,[53] the activation free energies calculated from first-principles MD simulations are higher than those obtained for the single-metal-ion model.[20] The lower activation barrier obtained in the present model agrees well with the experimental data and is likely to come from an optimal reaction pathway which was not sampled by Boero et al. It is noteworthy that the relative free energy difference between the noncatalyzed (no metal) and metal-catalyzed (two-metal-ion models) reactions is similar in the two models: it is 16.3 kcal/mol for Boero's model and 13.7 kcal/mol for our model.

3.6. Solvent Isotope Effect. The occurrence of a proton transfer during the rate-limiting step of the reaction is controversial. A large solvent deuterium isotope effect ($k_{cleav}^{(H_2O)}/k_{cleav}^{(D_2O)} = 4.3$) has been observed for the hammerhead ribozyme.[24] In the case of the participation of a metal hydroxide in the catalysis (Figure 1B), the observed isotope effect was imputed to a change in the equilibrium concentration of active species (Mg^{2+}-bound 2′ alkoxide).[24,54] Consequently, the isotope effect was not interpreted as a proton transfer occurring in the transition state (departure of the leaving group) but instead as an apparent isotope effect; that is, the isotope effect simply reflects a difference in the concentration of the activated 2′ oxyanion in D_2O (which is severalfold lower than that in H_2O) at a given pH.[17,24] Thus, the intrinsic isotope effect associated with the 2′ OH deprotonation would be equal to 1. However, experimental evidence supports the proton transfer when Mg^{2+} is substituted by NH_4^+ as a cofactor in the reaction.[35] To determine whether the two-metal-ion model proposed here is consistent with the observed isotope effect, we have used a simple model to estimate the kinetic solvent isotope effect (KIE) for the rate-determining (fourth) reaction step (Figure 3D).

Neglecting tunneling, the kinetic isotope effect can be approximated in transition state theory (TST) by the change in activation free energy of H_2O versus D_2O.[55] This gives

$$KIE_{cl} \simeq e^{(\Delta G_D^{\ddagger} - \Delta G_H^{\ddagger})/k_B T} \quad (1)$$

where $\Delta G^{\ddagger}$ is the barrier height corrected for zero-point-energy (ZPE) changes between the reactant (V, Figure 3D) and the transition state (VI, Figure 3D) in H_2O ($\Delta G_H^{\ddagger}$) and in D_2O ($\Delta G_D^{\ddagger}$) calculated at the HF/3-21+G** level (Supporting Information Table S2). The calculations give a KIE that is close to unity ($KIE_{cl} = 1.2$) and is consistent with the reaction asymmetry for this proton transfer.[55] This suggests that the KIE observed experimentally is likely to be due to a change in the equilibrium concentration of charged species in the presence of Mg^{2+}, as proposed earlier,[24,35] but that is not incompatible with a proton transfer to the leaving 5′ oxygen in the rate-limiting step of the reaction. In the case of a nucleophile activation model, based on a metal hydroxide at site I, an intrinsic KIE corresponding to a proton transfer on the 5′ oxygen, combined with a change in the equilibrium concentration of charged species, would lead to a much larger apparent KIE, as is observed for the NH_4^+-mediated reaction ($k_{cleav}^{(H_2O)}/k_{cleav}^{(D_2O)} = 7.68$.[35]

4. Concluding Discussion

A two-metal-ion model for hammerhead-ribozyme catalysis, based on density functional quantum mechanical calculations,

is described and analyzed. It is found that the reaction involves a series of steps with three intermediates and four transition states. The calculated free energy barriers for the solvated system (Table 2), confirmed by reaction path following (Supporting Information Figure S3), indicate that the intermediates involved in the first three steps of the reaction (nucleophile activation, nucleophilic attack, and formation of an intermediate involved in the departure of the leaving group) would have lifetimes too short to be kinetically significant; that is, the free energy barriers of the steps from the reactant to the final intermediate are all small, with the largest arising in the nucleophile activation (2.6 kcal/mol). The high free energy barrier which corresponds to the rate-determining step, involves the departure of the leaving group. The calculated free energy barrier (19.3 kcal/mol) is in good agreement with the measured value 20.1 kcal/mol. The high barrier is suggested to result from an "imbalanced" transition state; that is, there is an early destabilization of the last intermediate VII (due to the proton transfer from a coordinated water molecule at site II on the 5′ oxygen, Figure 3D), which occurs before the P−O5′ bond breaking, and a late stabilization of the product (due to the delocalization of the OH^- formed at site II and transferred to site I) that lags behind the breaking of the P−O5′ bond.

Comparison of a model for RNA catalysis corresponding to the base-catalyzed reaction in solution in the absence of metal ions (Leclerc et al., to be published separately) and the two-metal-catalyzed reaction in the hammerhead ribozyme, as obtained in the present paper, suggests that the metal ions contribute to the catalysis in several essential ways: (1) by lowering the pK_a of the 2′ OH, (2) by stabilization of the in-line conformation of the reactant, (3) by stabilization of the trigonal bipyramidal structure of the transition states and intermediates, and (4) by stabilization of the leaving group. One of the metal ions, identified as Mg_{II}, acts as a Lewis acid and a general acid, while the other metal ion, identified as Mg_I, functions as a general base and Lewis acid, so there is a clear distinction between the roles played by the two metals. Their roles as Lewis acids evolve along the reaction path; that is, a strong Lewis acid is needed at site I in the first steps (roles 1−3 described above) and at site II in the last steps of the reaction (roles 3 and 4 described above). The role of both metals as a Lewis acid is reinforced at site I by a pentacoordinated state of Mg_I in the two first steps of the reaction and at site II by a hexacoordinated state of Mg_I that contributes to delocalize the negative charge developed around the leaving group in the two last steps of the reaction. Given the above, we expect that any factor that minimizes the imbalance of the transition state in the rate-limiting step by making the proton transfer more synchronized with the P−O5′ bond breaking would accelerate the reaction. This can be accomplished, for example, by a later destabilization of the third intermediate (VII) or an earlier stabilization of the product (IX) with respect to the transition state (VIII‡). As proposed previously,[28] the presence of a stronger Lewis acid at site II would allow a better stabilization of the negative charge on the leaving group. In light of the present two-metal-ion model, the replacement of Mg^{2+} by La^{3+} at site II, which leads to an enhanced apparent rate constant for the hammerhead-ribozyme cleavage reaction,[28] lowers the energy barrier by a slightly earlier product stabilization (i.e., the P−O5′ bond would break earlier, making the departure of the leaving group more synchronized with the proton transfer) along the reaction pathway (likely by sequestrating the OH^- at site II).

In summary, the calculations presented here have provided a detailed reaction path for the two-metal-ion ribozyme catalysis and identified the metal-ion contribution to the reaction. Although the results are in agreement with experiments, additional measurements (KIE, for example) are necessary to confirm the analysis. We hope that having a specific proposal will stimulate new studies of this reaction, which is of fundamental importance in living systems.

Acknowledgment. The authors are grateful to Qiang Cui for many profitable discussions. We thank Eric Gledening and Baudilio Tejerina for technical support with the NBO program and Michael E. Harris for personal comments. F.L. was a fellow of the Human Frontier Science Program (1998−2000). This work was partially supported by grants from the Department of Energy (DOE, U.S.A.) and from the National Institute of Health (NIH) and by CNRS funding for young investigators (ATIP, France). The calculations were performed, in part, at the National Energy Research Scientific Computing Center (NERSC), at the Institut du Développement et des Ressources en Informatique Scientifique (IDRIS, France), and at the Centre Informatique National de l′Enseignement Supérieur (CINES, France).

Supporting Information Available: Detailed procedures for construction of guess geometries, geometry optimizations and energetics, location of transition state structures, and NBO and NEDA calculations. Data on the triester-like and dianionic mechanisms in solution and data on IRC calculations. Complementary data on the NEDA calculations of the three-body interactions and on the calculated barrier heights used to estimate the kinetic solvent isotope effect. This material is available free of charge via the Internet at http://pubs.acs.org.

References and Notes

(1) Cech, T.; Zaug, A.; Grabowski, P. *Cell* **1981**, *27*, 487−496.
(2) Zaug, A.; Cech, T. *Nucleic Acids Res.* **1982**, *10*, 2823−2838.
(3) Scott, W.; Murray, J.; Arnold, J.; Stoddard, B.; Klug, A. *Science* **1996**, *274*, 2065−2069.
(4) Scott, W.; Finch, J.; Klug, A. *Cell* **1995**, *81*, 991−1002.
(5) Murray, J.; Szoke, H.; Szoke, A.; Scott, W. *Mol. Cell* **2000**, *5*, 279−287.
(6) Murray, J.; Terwey, D.; Maloney, L.; Karpeisky, A.; Usman, N.; Beigelman, L.; Scott, W. *Cell* **1998**, *92*, 665−673.
(7) McKay, D. *RNA* **1996**, *2*, 395−403.
(8) Hammann, C.; Lilley, D. *ChemBioChem* **2002**, *3*, 690−700.
(9) Blount, K.; Grover, N.; Mokler, V.; Beigelman, L.; Uhlenbeck, O. *Chem. Biol.* **2002**, *9*, 1009−1016.
(10) Lilley, D. *Curr. Opin. Struct. Biol.* **1999**, *9*, 330−338.
(11) Fedor, M.; Uhlenbeck, O. *Biochemistry* **1992**, *31*, 12042−12054.
(12) van, T. H.; Buzayan, J.; Feldstein, P.; Eckstein, F.; Bruening, G. *Nucleic Acids Res.* **1990**, *18*, 1971−1975.
(13) Koizumi, M.; Ohtsuka, E. *Biochemistry* **1991**, *30*, 5145−5150.
(14) Slim, G.; Gait, M. *Nucleic Acids Res.* **1991**, *19*, 1183−1188.
(15) Raines, R. *Chem. Rev.* **1998**, *98*, 1045−1066.
(16) Wang, S.; Karbstein, K.; Peracchi, A.; Beigelman, L.; Herschlag, D. *Biochemistry* **1999**, *38*, 14363−14378.
(17) Kuimelis, R.; McLaughlin, L. *Biochemistry* **1996**, *35*, 5308−5317.
(18) Hermann, T.; Auffinger, P.; Scott, W.; Westhof, E. *Nucleic Acids Res.* **1997**, *25*, 3421−3427.
(19) Kuimelis, R.; McLaughlin, L. *Chem. Rev.* **1998**, *98*, 1027−1044.
(20) Torres, R.; Himo, F.; Bruice, T.; Noodleman, L.; Lovell, T. *J. Am. Chem. Soc.* **2003**, *125*, 9861−9867.
(21) Steitz, T.; Steitz, J. *Proc. Natl. Acad. Sci. U.S.A.* **1993**, *90*, 6498−6502.
(22) Uebayasi, M.; Uchimaru, T.; Koguma, T.; Sawata, S.; Shimayama, T.; Taira, K. *J. Org. Chem.* **1994**, *59*, 7414−7420.
(23) Dahm, S.; Derrick, W.; Uhlenbeck, O. *Biochemistry* **1993**, *32*, 13040−13045.
(24) Sawata, S.; Komiyama, M.; Taira, K. *J. Am. Chem. Soc.* **1995**, *117*, 2357−2358.
(25) Zhou, D.; Taira, K. *Chem. Rev.* **1998**, *98*, 991−1026.

(26) Pontius, B.; Lott, W.; von Hippel, P. *Proc. Natl. Acad. Sci. U.S.A.* **1997**, *94*, 2290−2294.
(27) Zhou, D.; Zhang, L.; Taira, K. *Proc. Natl. Acad. Sci. U.S.A.* **1997**, *94*, 14343−14348.
(28) Lott, W.; Pontius, B.; von Hippel, P. *Proc. Natl. Acad. Sci. U.S.A.* **1998**, *95*, 542−547.
(29) Lyne, P.; Karplus, M. *J. Am. Chem. Soc.* **2000**, *122*, 166−167.
(30) Nakamatsu, Y.; Warashina, M.; Kuwabara, T.; Tanaka, Y.; Yoshinari, K.; Taira, K. *Genes Cells* **2000**, *5*, 603−612.
(31) Zhou, J.; Zhou, D.; Takagi, Y.; Kasai, Y.; Inoue, A.; Baba, T.; Taira, K. *Nucleic Acids Res.* **2002**, *30*, 2374−2382.
(32) Curtis, E.; Bartel, D. *RNA* **2001**, *7*, 546−552.
(33) Murray, J.; Seyhan, A.; Walter, N.; Burke, J.; Scott, W. *Chem. Biol.* **1998**, *5*, 587−595.
(34) O'Rear, J.; Wang, S.; Feig, A.; Beigelman, L.; Uhlenbeck, O.; Herschlag, D. *RNA* **2001**, *7*, 537−545.
(35) Takagi, Y.; Inoue, A.; Taira, K. *J. Am. Chem. Soc.* **2004**, *126*, 12856−12864.
(36) Inoue, A.; Takagi, Y.; Taira, K. *Nucleic Acids Res.* **2004**, *32*, 4217−4223.
(37) Zhou, D.; He, Q.; Zhou, J.; Taira, K. *FEBS Lett.* **1998**, *431*, 154−160.
(38) Scott, E.; Uhlenbeck, O. *Nucleic Acids Res.* **1999**, *27*, 479−484.
(39) Murray, J.; Dunham, C.; Scott, W. *J. Mol. Biol.* **2002**, *315*, 121−130.
(40) Bock, C.; Kaufman, A.; Glusker, J. *Inorg. Chem.* **1994**, *33*, 419−427.
(41) Cunningham, L.; Li, J.; Lu, Y. *J. Am. Chem. Soc.* **1998**, *120*, 4518−4519.
(42) Scott, A.; Radom, L. *J. Phys. Chem.* **1996**, 100, 16502−16513.
(43) Marten, B.; Kim, K.; Cortis, C.; Friesner, R.; Murphy, R.; Ringnalda, M.; Sitkoff, D.; Honig, B. *J. Phys. Chem.* **1996**, *100*, 11775−11788.
(44) Zhou, D.; Usman, N.; Wincott, F.; Matulic-Adamic, J.; Orita, M.; Zhang, L.; Komiyama, M.; Kumar, P. K. R.; Taira, K. *J. Am. Chem. Soc.* **1996**, *118*, 5862−5866.
(45) Bash, P.; Field, M.; Davenport, R.; Petsko, G.; Ringe, D.; Karplus, M. *Biochemistry* **1991**, *30*, 5826−5832.
(46) Gonzalez, C.; Schlegel, H. *J. Phys. Chem.* **1990**, *94*, 5523−5527.
(47) Scott, W. *Q. Rev. Biophys.* **1999**, *32*, 241−284.
(48) Glendening, E.; Badenhoop, J.; Reed, A.; Carpenter, J.; Bohmann, J.; Morales, C.; Weinhold, F. Theoretical Chemistry Institute, University of Wisconsin, Madison, 2001.
(49) Vishveshwara, S.; Madhusudhan, M.; Maizel, J. J. *Biophys. Chem.* **2001**, 89, 105−117.
(50) Gerlt, J.; Gassman, P. *J. Am. Chem. Soc.* **1993**, *115*, 11552−11568.
(51) Gerlt, J.; Gassman, P. *Biochemistry* **1993**, *32*, 11943−11952.
(52) Boero, M.; Terakura, K.; Tateno, M. *J. Am. Chem. Soc.* **2002**, *124*, 8949−8957.
(53) Boero, M.; Tateno, M.; Terakura, K.; A, O. *J. Chem. Theory Comput.* **2005**, *1*, 925−934.
(54) Takagi, Y.; Taira, K. *J. Am. Chem. Soc.* **2002**, *124*, 3850−3852.
(55) Kiefer, P.; Hynes, J. *J. Phys. Chem.* **2003**, *107*, 9022−9039.

Supporting Information

Mono- and dianionic Reaction Mechanisms in Solution

The reactions in solution under acid (Fig. S1) or basic (Fig. S2) conditions, corresponding to the 'triester-like' and dianionic mechanisms respectively, are described below.

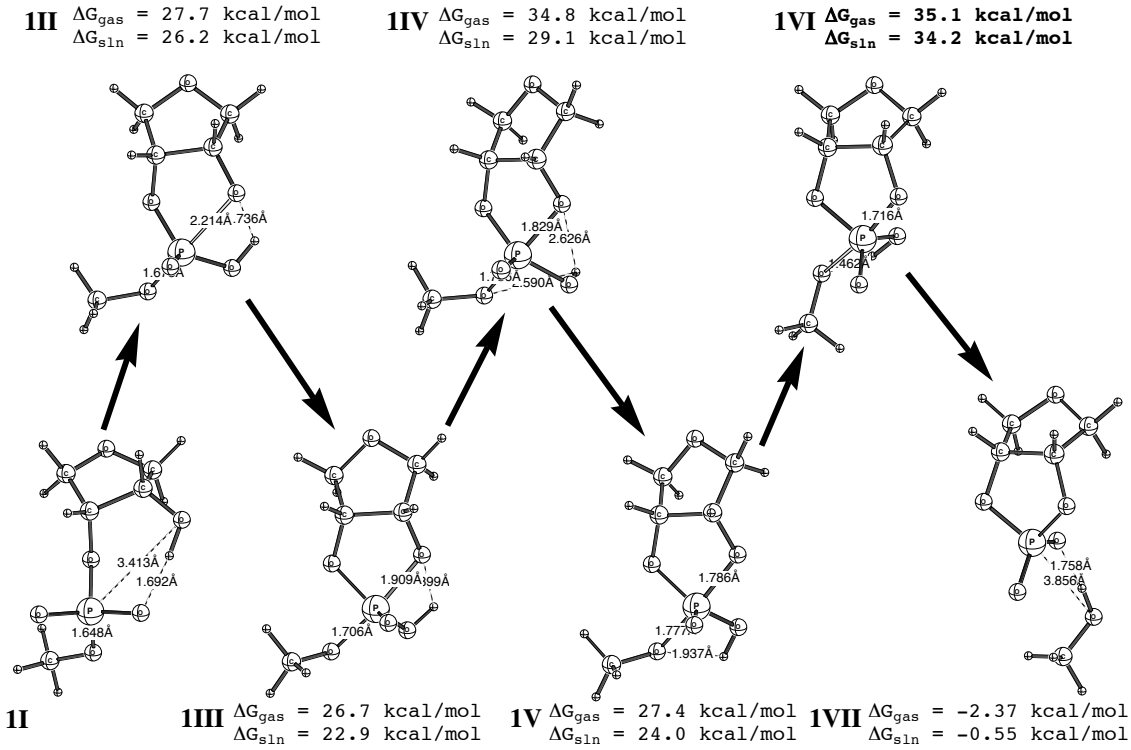

Figure S1: 'Triester-like' reaction mechanism. The geometries of the stationary points are optimized at the B3LYP/6-31+G**//B3LYP/6-31+G** level; the free energies calculated using the reactant (1I) as reference are given at the same level. The relative free energies in solution (ΔG_{sln}) inlude a correction for the solvation free energy calculated using the PCM model. The relative free energies indicated in bold correspond to the rate-limiting step of the reaction.

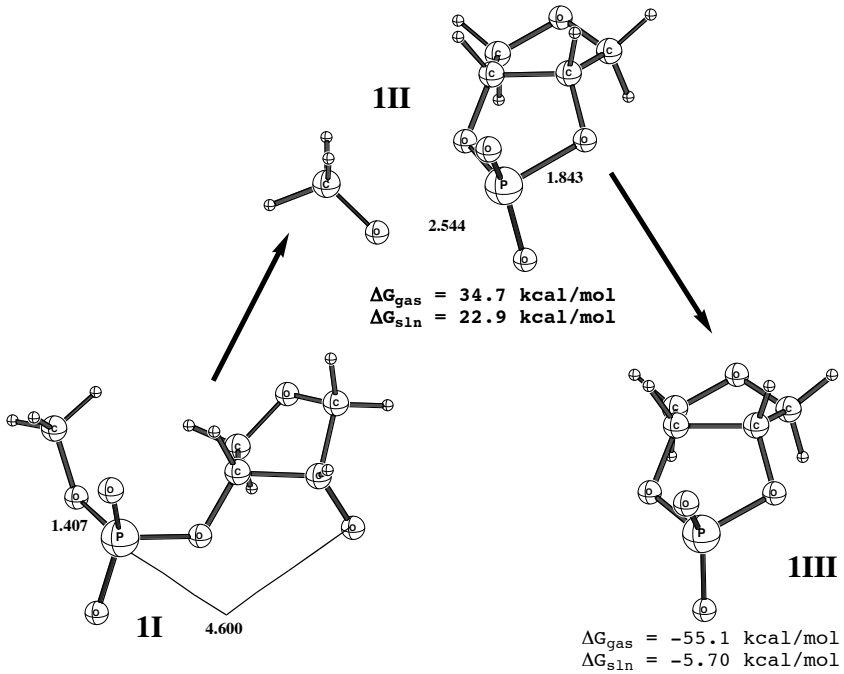

Figure S2: Dianionic reaction mechanism. The geometries of the stationary points are optimized at the B3LYP/6-31+G**//B3LYP/6-31+G** level; the free energies calculated using the reactant (1I) as reference are given at the same level. The relative free energies in solution (ΔG_{sln}) inlude a correction for the solvation free energy calculated using the PCM model. The relative free energies indicated in bold correspond to the rate-limiting step of the reaction.

Construction of guess geometries

Ten different starting geometries were generated for a phosphorylated ribose in a conformation amenable to an 'in-line' attack. The geometry of the phosphorylated ribose was taken from that of a small RNA model (Leclerc *et al.*, to be published separately) and two solvated metal ions hexa- or pentacoordinated were merged to the RNA. Before optimization, the guess geometries exhibit: (1) conserved inner sphere coordinations with the 2'-oxygen and the 5'-oxygen (in agreement with the two-metal-ion model), (2) variable inner or outer sphere coordinations with the nonbridging pro-Rp and/or pro-Sp oxygens at the first metal site (2'-oxygen) and with the pro-Rp oxygen at the second metal site (5'-oxygen). After optimization with frozen internal coordinates corresponding to the O2'-P and P-O5' distances, only 7 different guess geometries were obtained; three out of

the initial 10 geometries did converge to existing geometries. Among these 7 geometries, four were potential transition states (presence of an imaginary frequency) corresponding to either the nucleophilic attack of the O2' oxygen on the phosphorus (2 geometries), the departure of the leaving group (1 geometry) or both (1 geometry).

During the optimizations with frozen internal coordinates, a coordination change at the metal site I was observed for one of the two geometries corresponding to a potential transition state for the nucleophilic attack and for the one corresponding to the concerted mechanism as well (nucleophilic attack and departure of the leaving group). This coordination change from a hexa- to pentacoordinated form is correlated to a more favorable 'in-line' conformation for the nucleophilic attack. Among the three geometries corresponding to potential transition states for the nucleophilic attack, two exhibit a pentacoordinated form at the metal site I and a O2'-P-O5' angle more than 160° (161 and 162°), the remaining one is hexacoordinated and exhibit a O2'-P-O5' angle of 148° more distant with respect to the ideal 'in-line' conformation. After full optimizations with unfrozen coordinates, only two geometries were found to correspond to two separate transition states related to the nuleophilic attack and departure of the leaving group. The transition state corresponding to the nucleophilic attack exhibits a pentacoordinated metal at site I while both metals are hexacoordinated in the case of the transition state corresponding to the departure of the leaving group.

Geometry Optimizations and Energetics

All geometry optimizations were performed using Gaussian98 (Gaussian, Inc., Pittsburgh PA, 2001, Revision A.10). The frequencies were scaled by an empirical factor of 0.9207 to correct, at the HF/3-21+G* level, for errors in the potential energy surface.[42] The free energies were calculated from the frequencies for the following contributions by adding

the entropy, zero-point energy and vibrational energy at 298K to the quantum mechanical energy. The other contributions (rotational and translational energies, and work term (PV)) were calculated according to standard classical statistical mechanics (an ideal gas PV term was added to obtain the Gibbs free energy). Effective energies in solution (in pure solvent) were calculated for the geometries optimized in the gas phase using the solvation model (Poisson-Boltzmann solver) implemented in Jaguar (Jaguar, Schrödinger, Inc., 2002, version 4.2).[43]

Location of Transition States Structures and Reaction Path Following

The transition structures were obtained from a series of guess geometries constructed using different reaction coordinates defined by the O2'-P and P-O5' distances and inferred from the calculations on a metal-free model. The transition structures were located using standard geometry optimization methods, except the transition structure corresponding to the change in the metal coordinations at site I (Fig. 3C). This latter transition structure was located using the Synchronous Transit-guided Quasi-Newton (STQN) method (Gaussian 98) using the structures from both intermediates (V and VII, Fig. 3B and 3C).

The reaction path derived from IRC calculations is shown below.

A)

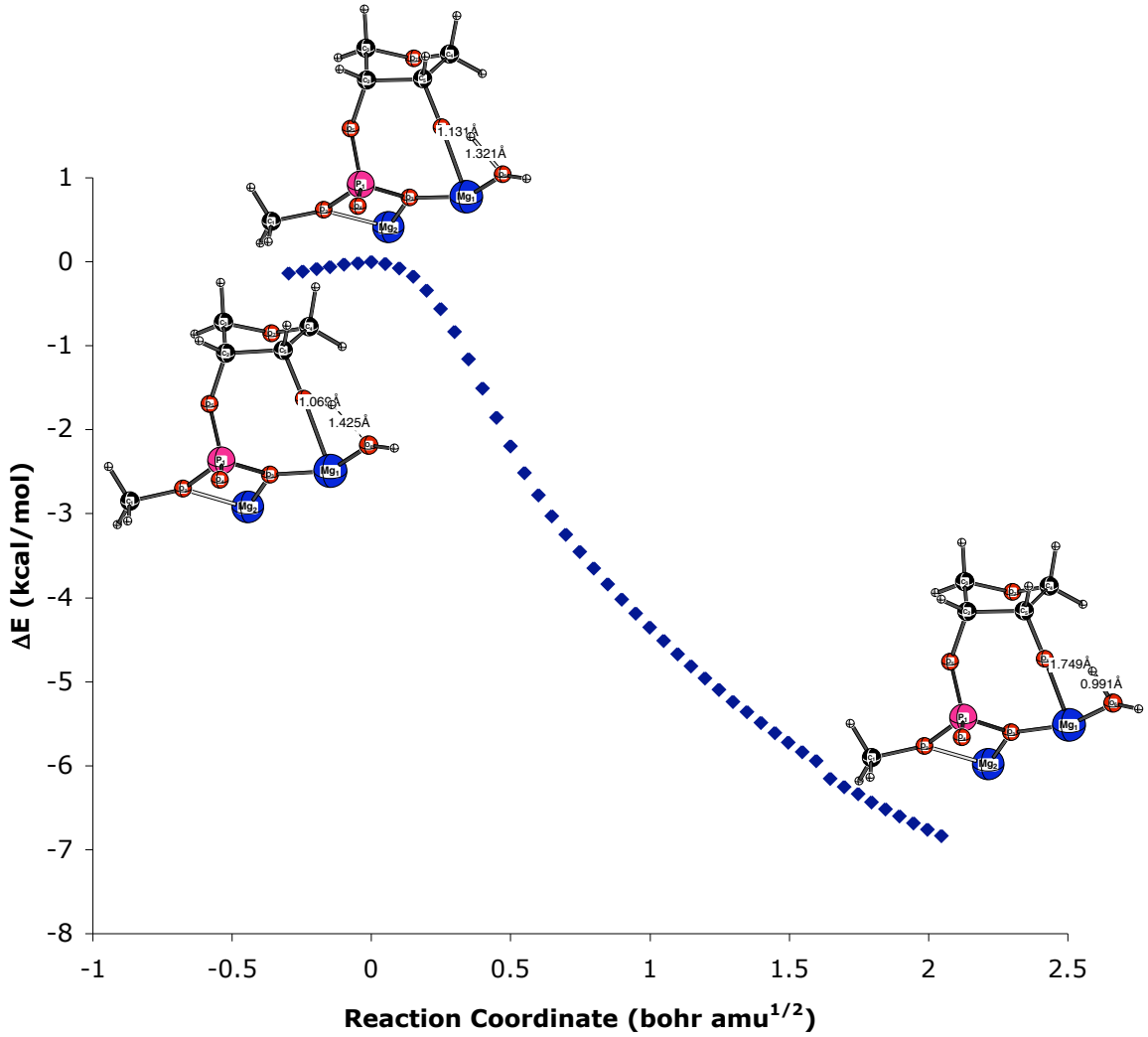

Figure S3: Dianion/3-21+G* IRC calculations: (A) for the first transition state (I), (B) for the second transition state (II), (C) for the third transition state (IV) and (D) for the fourth transition state (VI). The transition state and end points of the IRC are shown with the distances between the nucleophile (O2') and the phosphorus and between the phosphorus and the leaving group (O5'). Only the relevant water molecules are shown in each reaction step. The reference for the relative energy corresponds to the first transition state (A); the relative energies are given with respect to this reference in (B), (C) and (D).

B)

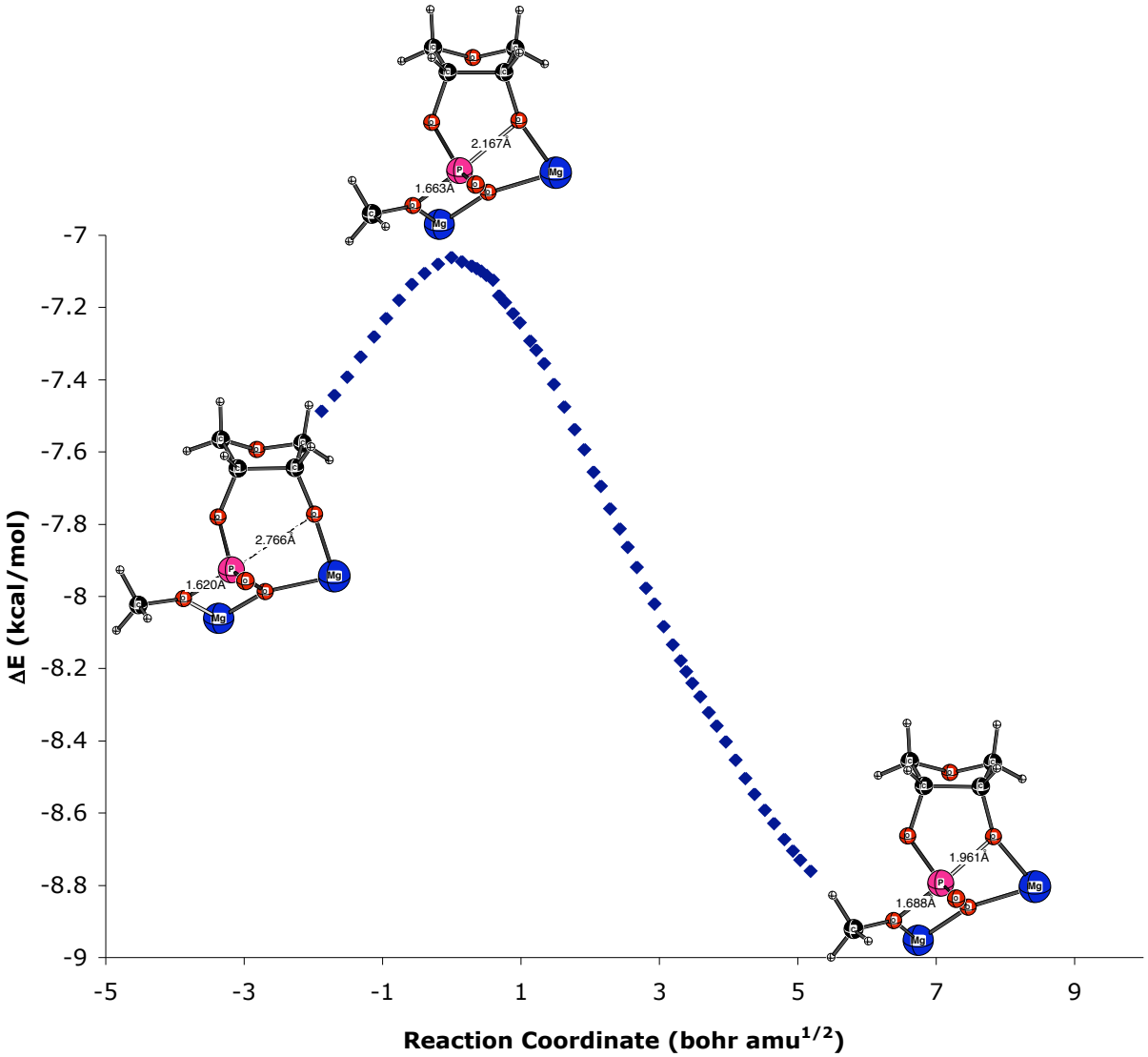
2.167Å
1.663Å
2.766Å
1.620Å
1.961Å
1.688Å
-7
-7.2
-7.4
-7.6
-7.8
-8
-8.2
-8.4
-8.6
-8.8
-9
ΔE (kcal/mol)
-5
-3
-1
1
3
5
7
9
Reaction Coordinate (bohr amu1/2)

Figure S3 (B)

C)

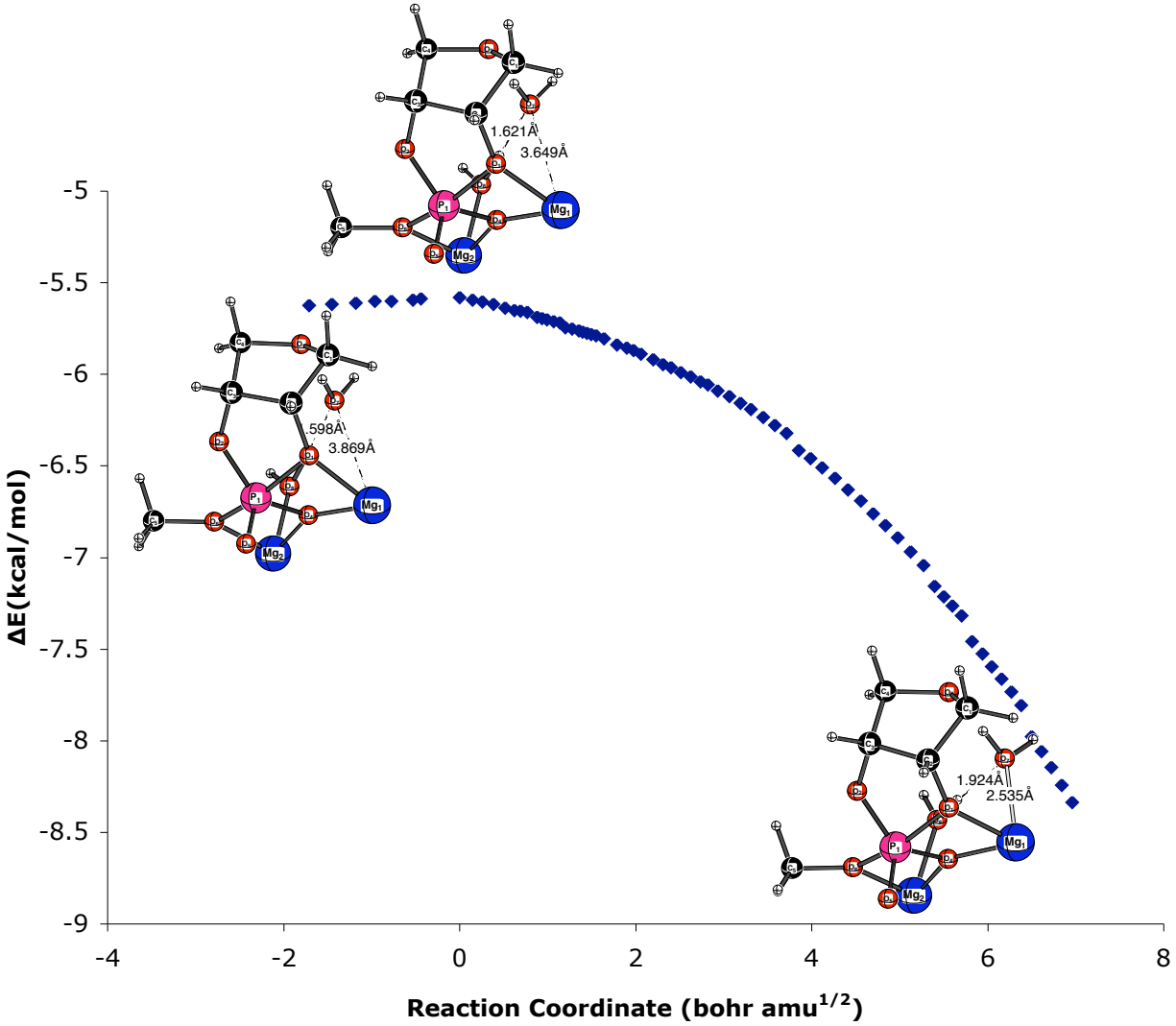
1.621Å
3.649Å
1.598Å
3.869Å
1.924Å
2.535Å
ΔE(kcal/mol)
-5
-5.5
-6
-6.5
-7
-7.5
-8
-8.5
-9
-4
-2
0
2
4
6
8
Reaction Coordinate (bohr amu^1/2)

Figure S3 (C)

D)

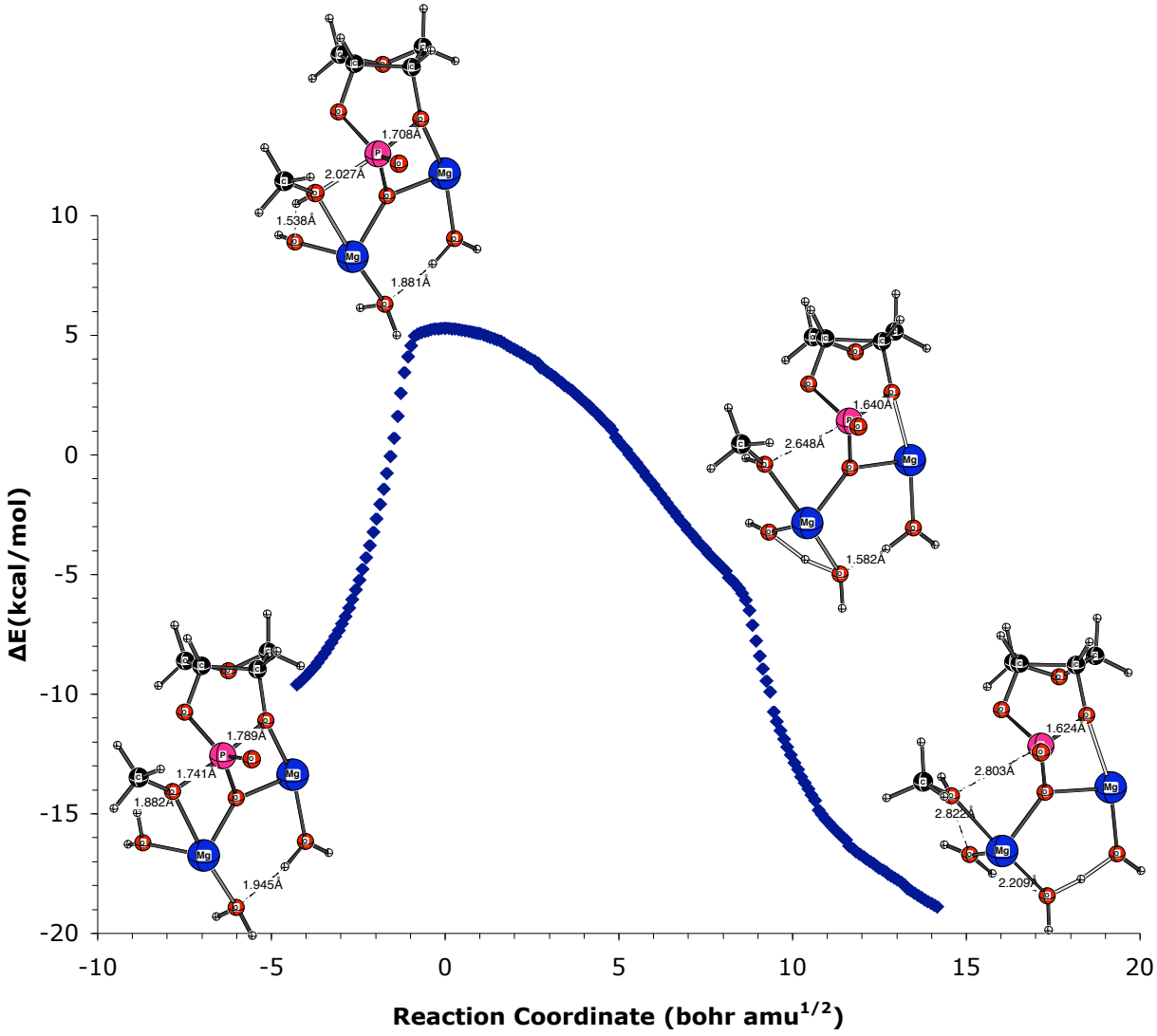
ΔE(kcal/mol)
Reaction Coordinate (bohr amu^1/2)
10
5
0
-5
-10
-15
-20
-10
-5
0
5
10
15
20
1.708Å
2.027Å
1.538Å
1.881Å
1.640Å
2.648Å
1.582Å
1.789Å
1.741Å
1.882Å
1.945Å
1.624Å
2.803Å
2.822Å
2.209Å

Figure S3 (D)

NBO and NEDA Calculations

The natural bond orbital (NBO) and natural energy decomposition analyses (NEDA) were performed at each stationary point at the B3LYP/6-31+G**//HF/3-21+G* and HF/6-31+G**//HF/3-21+G* levels, respectively. The NBO program (version 5.0)[48] implemented in the GAMESS(US) program was used for both NBO and NEDA analyses.

The binding energy can be decomposed into two-body interactions between pairs of fragments (RNA-Mg_I, RNA-Mg_{II}, Mg_I-Mg_{II}, and a non-pairwise additive three-body interaction:

$$\Delta E = \Delta E(RNA - Mg_I) + \Delta E(RNA - Mg_{II}) + \Delta E(Mg_I - Mg_{II}) + \Delta E(3 - body) \quad (2)$$

Each term can be partitioned into electrostatic (ES), polarization (POL), charge transfer (CT), exchange (EX) and deformations contributions (DEF).

Table S1. Natural energy decomposition analyses (NEDA) of the Three-Body interactions[a].

	three-body term RNA+Mg_I+Mg_{II}				
Molecule	ΔE^b_{tot}	POL	CT	EX	DEF
I	6.97	18.6	2.88	1.78	-16.7
II	4.72	17.2	1.45	1.94	-16.2
III	22.3	38.4	12.9	0.93	-30.0
IV	24.6	41.6	13.3	1.12	-31.4
V	26.4	44.6	14.4	1.43	-34.0
VI	23.5	36.6	15.4	1.29	-29.8
VII	22.3	32.8	16.6	1.37	-28.5
VIII	12.8	20.1	7.10	1.10	-15.5
IX	15.2	13.0	-12.7	-0.1	15.0

[a] RHF/6-31+G*//RHF/3-21+G* values in kcal/mol. The binding energy calculated as previously (Table 4) is decomposed into two-body interactions between pairs of fragments (Table 5) and a non-pairwise-additive three-body term.

Table S2. Solvent deuterium KIE[a].

$\Delta G^{\ddagger}_H$ [b]	$\Delta G^{\ddagger}_D$ [c]	KIE_{cl}
20.1	20.2	1.22

[a] RHF/3-21+G* values in kcal/mol at 298K. [b] barrier height corrected for ZPE changes in H_2O. [c] barrier height corrected for ZPE changes in D_2O.